Wireless Biodegradable Resonant circuit for Strain Sensor in Hip Implant applications

by

Student Name	Student Number
Nikita Gopakumar	5221234

to obtain the degree of Master of Science in Biomedical Engineering
at the Delft University of Technology.

Student number:	5221234	
Thesis committee:	Prof. J. Zhou,	TU Delft, supervisor
	Prof. C. Boutry,	TU Delft, supervisor
	Prof. Y. Aslan,	TU Delft, supervisor

TU Delft

Acknowledgements

I am deeply grateful for the invaluable support and guidance provided by Prof. J. Zhou, Prof. C. Boutry, and Prof. Y. Aslan, my esteemed supervisors. Their unwavering assistance and counsel have greatly enhanced my journey.

Their willingness to meet and assist whenever required has immensely enriched my learning experience. Their confidence in my work and their commitment to my success have profoundly influenced me, leaving a lasting impression that I will always remember.

Abstract

Hip replacement surgery, also termed total hip arthroplasty, is a surgical intervention intended to substitute a deteriorated or dysfunctional hip joint with an artificial prosthesis. This procedure is commonly indicated for individuals experiencing severe hip discomfort resulting from conditions like osteoarthritis, rheumatoid arthritis, hip fractures, or other hip-related issues that significantly impair mobility.

Globally, more than 1 million total hip replacement surgeries are conducted annually. Given the substantial mechanical loads experienced by hip implants during regular activities, a thorough understanding and early identification of potential issues before implant failure are imperative. Continuous monitoring of strain is crucial to assess how the implant responds to various stresses over time. This monitoring aids in evaluating the implant's durability and performance under diverse stress conditions, enabling proactive interventions, if necessary, to prevent critical failures.

Strain monitoring acts as a diagnostic tool to assess the implant's status and the surrounding tissues. Deviations in strain patterns may signify problems such as implant loosening, wear, or bone loss around the implant. Moreover, this monitoring technique helps customize rehabilitation programs and recommend specific activities based on individual strain levels. Consequently, this tailored approach enhances recovery outcomes while mitigating associated risks.

This project involves the development of a passive wireless resonant circuit that will be used in the future in a sensor designed to detect strain on hip implants for early failure detection. The strain is anticipated to cause fluctuations in the frequency. To evaluate the LC (inductor-capacitor) resonator design at a specific frequency, a simulation model was established using the Computer Simulation Technology (CST) Microwave Studio as the simulation platform. The fabrication of this LC resonant circuit employs cleanroom techniques and protocols to ensure precision and reliability in its structure. Subsequent to fabrication, the resonator underwent characterization employing an antenna to ascertain resonance frequency alterations in accordance with theoretical expectations. The results indicated a detectable shift in resonant frequency corresponding to designs representing different strains.

Contents

List of Figures

List of Tables

Nomenclature

Abbreviations

Abbreviation	Definition
PLA	poly-lactic acid
PGA	polyglycolic acid
PHB	poly-β-hydroxybutyrate
PLGA	poly (lactic acid-co-glycolic acid)
PCL	poly-ϵ-caprolactone
PGS	poly(glycerol sebacate)
POMaC	poly(octamethylene maleate (anhydride) citrate)
PVA	polyvinyl alcohol
PMMA	polymethyl methacrylate
PI	polyimide
BTE	Bone tissue engineering
AM	Additive Manufacturing
Mg	Magnesium
Fe	Iron
Zn	Zinc
Mo	Molybdenum
AlN	Aluminum Nitride
SAW	Surface Acoustic Wave
IoT	Internet of Things
LoSD	Limit of Strain Detection
SNR	Signal-to-Noise ratio
AgNW/CNF	Ag nanowire/cellulose nanofibril
AuNPs	Gold nanoparticles
ICs	Integrated circuits
PECVD	Plasma-enhanced Chemical Vapor Deposition
LC circuit	Inductor-Capacitor circuit
CST	Computer Simulation Technology Studio Suite

1

Introduction

1.1. Hip replacement surgery

The hip constitutes a complex system within the human body, comprising a strong joint that links the pelvis to the thigh bone. It functions as a ball and socket joint, where the rounded head of the femur bone fits into the cup-shaped acetabulum of the pelvis (Figure 1.1). This joint is enveloped by a robust capsule supported by a network of ligaments, tendons, and muscles. Being a synovial joint, it contains synovial fluid, which serves to lubricate, nourish the joint surfaces, and diminish friction and wear between bones during movement [1].

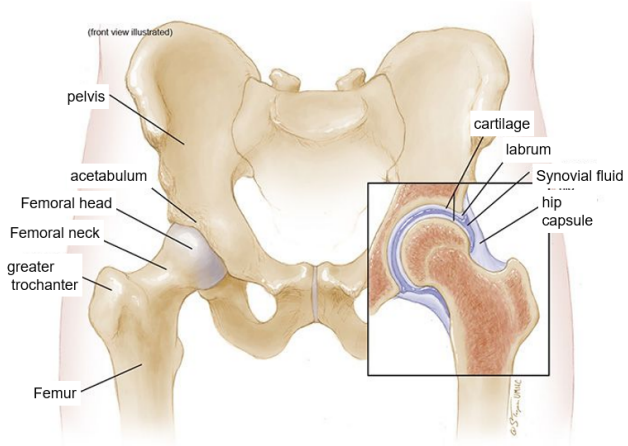

Figure 1.1: Anatomy of a hip joint [2].

Furthermore, the hip joint plays a crucial role in bearing weight and maintaining stability by supporting the body's weight while facilitating an extensive range of motions. A comprehensive understanding of the hip joint's anatomy is essential for accurately diagnosing and effectively treating injuries and conditions related to the hip. Various conditions affecting the hip joint encompass osteoarthritis, rheumatoid arthritis, and hip fractures. Injuries to this joint can result from trauma, repetitive strain, or degenerative alterations. Osteoarthritis, a degenerative joint ailment impacting joint cartilage, is the most prevalent form of arthritis, commonly affecting weight-bearing joints like hips, knees, and the spine. The estimation suggests that around 240 million individuals worldwide are affected by osteoarthritis [3]. Treatments for

hip-related issues may involve physical therapy, medication, or surgery, depending on the condition's severity and characteristics [4].
In some instances, surgical intervention might be necessary, entailing the replacement of the damaged joint with an artificial one. Hip replacement surgery involves removing and substituting parts of the pelvis and femur (thighbone) that constitute the hip joint [5]. It is estimated that approximately 1 million total hip replacements are performed worldwide each year [6]. Typically used to address hip pain and stiffness arising from hip arthritis, partial hip replacement, known as hemiarthroplasty, involves replacing only one side of the hip joint—the femoral head—unlike the total hip replacement, which involves both sides. Components of the hip implant are shown in Figure 1.2.

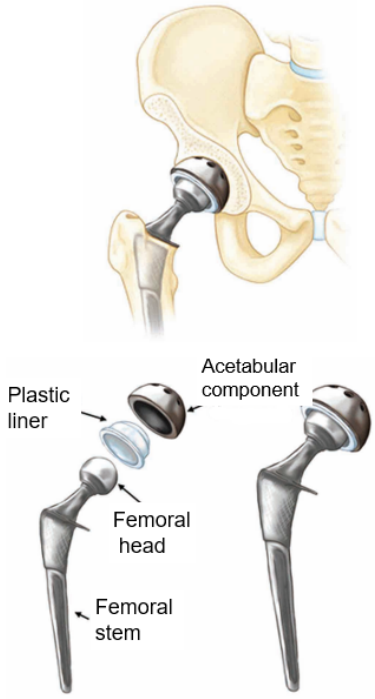

Figure 1.2: Components of the hip implant.

1.2. Hip implants failure

Failures in hip implants can occur due to various reasons, leading to patient discomfort and complications, and requires revision surgeries. It was indicated that close to 10% of primary joint implants necessitated revision interventions [7]. The poor fixation between the implant and the bone can result in loosening of the implant [8]. This can occur due to inadequate initial stability, bone resorption (osteolysis), or the breakdown of the bond between the implant and bone over time.

1.3. Biodegradable hip implants

1.3.1. The need for partial biodegradable implants

Hip implants commonly comprise metallic elements such as chromium, cobalt, molybdenum, nickel, titanium, and zirconium oxide. There have been complaints regarding metal implant failures and metal-related allergies [7]. As outlined in Section 1.2, complications including metal allergies, stress shielding, and long-term risks linked with permanent implants can potentially be mitigated by substituting (partial) sections of the permanent implants with biodegradable materials, specifically the components such as the femoral stem inserted into the bone or the peripheral layer of the femoral stem.

1.3.2. Biodegradable materials for implants

Biodegradable materials find common application in bone implants, fracture mending, and bone defect remediation [9]. Biodegradable metals are specifically engineered to disintegrate within the body, obviating the necessity for surgical extraction post-healing. Examples of such materials include magnesium-based alloys and iron-based alloys, which degrade at a pace compatible with tissue regeneration. These metals are selected for their mechanical strength and compatibility with bone healing processes [10]. Biodegradable polymers are large molecules capable of undergoing decomposition through natural biological processes. They consist of covalently bonded monomers, with compositions that can be either natural, such as starch, or synthetic such as poly-lactic acid (PLA). The commonly used biodegradable polymers are polyglycolic acid (PGA), polylactic acid (PLA), poly-β-hydroxybutyrate (PHB), poly (lactic acid-co-glycolic acid) (PLGA) and poly-ϵ-caprolactone (PCL) [9].

1.3.3. State-of-the-art biodegradable hip implants

As mentioned in section 1.3.1 biodegradable materials have the potential to promote bone cell growth, which helps to reduce the complications related to implant failure [11]. It is seen that magnesium and its alloys are favored for bone regeneration due to their biocompatibility, suitable mechanical strength, and biodegradability. They are lightweight with a density similar to human cortical bone and have a lower elastic modulus than titanium alloy and stainless steel, minimizing stress shielding effects. The biodegradability of magnesium allows it to degrade in the body.

X. Wang et al. (2016) provided an overview of advancements in topological design and additive manufacturing of porous metals for bone scaffolds and orthopaedic implants. The study focuses on customizing mechanical properties and improving osseointegration. Additive manufacturing serves as a disruptive technology for fabricating orthopaedic implants with intricate internal architectures. It also emphasizes the necessity for post-treatment and surface modification to enhance mechanical and biological performance and identifies challenges and future directions for integrating topology optimization with additive manufacturing. Their analysis highlights the promise of porous metals, especially titanium alloys, biodegradable metals, and shape memory alloys, for bone scaffolds and orthopaedic implants. Additive manufacturing facilitates the creation of intricate structures with tailored mechanical performance. Integrating topology optimization with additive manufacturing stands as a vital area of research interest for developing structures for bone tissue repair [12].

X. Zhang et al. (2017) examined the utilization of additive manufacturing (AM) in crafting bone tissue engineering (BTE) scaffolds, primarily focusing on metallic biomaterials and predicting their mechanical behavior through finite-element analysis. Practical applications include advancing the development of personalized implants with specific mechanical properties, enhancing integration with bone tissue. It also establishes a predictive framework for scaffold performance, reducing the necessity for extensive experimental testing. Additionally, it aids in guiding the selection of AM methods and materials to create scaffolds possessing desired porosity and mechanical strength [13].

Additive manufacturing (AM) represents a major leap forward in producing tailored biomaterials and sophisticated devices with intricate structures and adaptable properties, crucial for biomedical implants. These biomaterials encompass biodegradable polymer-based and metal-based materials. However, their degradation rate depends on environmental conditions and alloy types, necessitating safety measures and process alterations during AM, particularly for magnesium alloys. Utilizing biodegradable materials for implants that promote natural bone growth may face cytotoxicity challenges during degradation. Conversely, biocompatible metals and alloys like titanium and its derivatives, known for excellent corrosion resistance and exceptional mechanical properties, find widespread biomedical use.

AM revolutionizes biomaterial production by enabling intricate internal microstructure designs, especially porous lattice structures for tissue engineering and regenerative medicine. It allows diverse material utilization, enhancing their physical, mechanical, and biological attributes for varied medical applications and holds potential for cost-effective advanced biomedical device production.

Biomedical polymers suitable for AM must be biocompatible and biodegradable for tissue regeneration. Synthetic polymers offer better stability and slower degradation than natural polymers. Understanding the fatigue behavior of 3D-printed polymeric materials is crucial for ensuring medical device durability. In conclusion, AM transforms biomaterial production, but each method has specific limitations and advantages in medical device fabrication. Designing microarchitectural structures, especially porous architectures in biomaterials, is essential for efficient nutrient and oxygen transport. Future research should enhance biomaterial longevity and biocompatibility, exploring multi-material printing and improved joining methods for biomaterials [14].

The current landscape of additively manufactured biodegradable porous metals designed for bone implants, concentrating on their mechanical attributes, biodegradation, biocompatibility, and bone regeneration efficacy is examined [15]. It delves into the effects of material type, processing techniques, and design on the mechanical properties and degradation behavior of AM porous metals, exploring the *in vitro* biocompatibility and *in vivo* bone regeneration performance of AM porous metals such as Mg, Fe, Zn, and their alloys. Identifying gaps and challenges in their adoption for orthopedic applications, Y. Li et al. (2020) proposed future research avenues aimed at refining the properties and performance of AM biodegradable porous metals. Their findings underscored the capacity to tailor AM biodegradable porous metals, like Mg, Fe, and Zn, for bone implants, exhibiting favorable mechanical properties and degradation rates. Porous structures facilitate cell adhesion and proliferation, aiding bone ingrowth.

Notably, magnesium and zinc displayed superior *in vitro* biocompatibility, compared to iron. The impact of biodegradation on fatigue behavior was evident, with magnesium and iron experiencing decreased fatigue life, while zinc demonstrated increased fatigue life after immersion. Their conclusions suggest that AM biodegradable porous metals hold promise as substitutes for bone implants, with their functionality amenable to enhancement through proper design and treatment. Optimization of mechanical properties via AM processes, alloying, and design is feasible. The complexity of biodegradation behavior could potentially be addressed through various influencing factors, possibly leveraging predictive modeling aided by machine learning. Notably, *in vitro* biocompatibility, influenced by ion release, indicates better outcomes for magnesium and zinc compared to iron. Bridging the gap between laboratory findings and clinical performance warrants essential *in vivo* studies [16].

The advancements in 3D printing techniques concerning biodegradable metals used in orthopedic implants, highlighting their clinical implications and potential applications in tissue engineering and regenerative medicine were mainly reported by Sekar et al. (2021). The employment of 3D printing technology facilitates the fabrication of personalized orthopedic and dental implants, thereby enhancing individualized healthcare outcomes. The ongoing research and development surrounding biodegradable metals such as magnesium, calcium, zinc, and iron for implantation purposes suggest a potential reduction in long-term complications across various medical domains. Moreover, the integration of medical imaging modalities with additive manufacturing techniques allows for the precise and tailored production of implants, catering to the specific needs of individual patients. The effective utilization of 3D printing technology with biodegradable metals has been observed within the orthopedic disciplines, particularly in the creation of implants customized to meet individual patient needs. Promising biodegradable materials, including magnesium, calcium, zinc, and iron, have been identified for diverse biomedical applications [17].

Wegener et al. (2020) focused on an investigation to emphasize the development of biodegradable porous iron-based implants intended for bone replacement, engineered to withstand considerable mechanical loads and promote bone growth within its framework. The creation of Fe0.8P-based porous implants demonstrates promise in bone regeneration, facilitating bone tissue assimilation into the implant's structure. Modifications to both the alloy composition and the implant's structure are essential to hasten degradation and amplify bone integration, rendering the implant clinically viable. The implant's potential to provide primary stability for substantial bone defects could potentially transform treatment modalities in bone replacement surgeries. Manufactured open-cell metallic implants with variable densities, measuring 1.0 and 1.4 g/cm³, corresponded to porosities of 87% and 82%, respectively. The implants exhibited a pearlitic-ferritic microstructure characterized by uniformly dispersed phosphorus. The implants demonstrated compressive strengths of 13.1 MPa and 22.8 MPa and Young's moduli measuring 0.8 and 1.3 GPa, respectively [18].

The design of a biodegradable implant plate for femoral shaft fracture was reported by Chandra et al. (2020). It utilizes computational structural analysis to confirm the safety of the implant plate design. The study investigates the topological optimization of the implant plate to minimize stress and material without compromising functionality and analyzes the stresses generated on the implant plate under loading conditions and during the degradation process.The

implant plate breaks down entirely within 3 to 6 months after the healing process finishes, and the thickness of the plate becomes notably influential during this degradation period. These optimized biodegradable implants can reduce the need for second surgery to remove hardware after bone healing and the use of Mg-alloys in implants offers potential nutritional benefits and mechanical stability during the healing process [19].
The development of a biodegradable, iron-based, porous implant for bone replacement that can bear mechanical loads and degrade over time is studied. With the initial animal model tests, it shows bone integration and signs of degradation. However, it takes over 12 months for complete degradation. There is no inflammatory reactions observed up to 12 months which shows that the implant is biocompatible [18].

The research developed a magnesium-matrix composites with bredigite to control degradation and enhance bioactivity for bone implants. The composites showed degradation rates, maintained mechanical integrity, and stimulated bone cell responses, as compared to magnesium. The bredigite in the composites enhanced early cell attachment which was indicated by the presence of cytoplasmic extensions and had stimulatory effects on cell proliferation. The magnesium-matrix composites with bredigite can be produced with strengths comparable to cortical bone. The composites exhibit a significantly reduced biodegradation rate, thereby enhancing their longevity in orthopedic applications. The improved cell viability and proliferation indicate potential for better bone integration and healing [20].

Additively manufactured porous iron with graded porosity for potential use as a biodegradable biomaterial was studied. Porous iron exhibiting graded porosity has an influence on its mechanical properties and degradation behavior. It is these graded structures that can maintain necessary mechanical support while enhancing biodegradation and mass transport. The permeability is highly dependent on the porosity and specific surface area of the structure. The various incompatible design requirements for bone substitutes were met by utilizing graded designs, which demonstrated the potential of inexpensive pure iron for biodegradable metal applications. The use of porous iron enables making or designing of bone substitutes to match its biodegradation rates to the healing processes of natural bone. It also demonstrates cytocompatibility that is essential for biomedical applications [21].

The exploration of biodegradable materials, particularly metals and their alloys like magnesium, iron, zinc, and their composites, underscores their potential for orthopedic implants and bone tissue engineering. The studies highlight their favorable biocompatibility, the ability to tailor mechanical properties through additive manufacturing, and the creation of porous structures for better bone integration. Nevertheless, there are evident gaps in addressing challenges related to degradation rates, ensuring sustained biocompatibility during degradation, and effectively translating laboratory findings into clinical performance. These gaps serve as significant motivations for further research and development in biomedical engineering to enhance personalized implant technology, minimize complications, and advance healing processes in orthopedic applications.

1.4. Motivation of the project

Monitoring strain in hip implants is crucial due to the considerable mechanical stress they endure during everyday activities. Understanding potential issues before implant failure is paramount, necessitating a comprehensive grasp and early detection of problems. Continuous strain monitoring becomes vital to assess how the implant responds to various loads over time, determining its durability and performance under diverse stress conditions. This proactive monitoring allows for timely interventions to prevent critical failures.

Assessing strain serves as a diagnostic tool to evaluate both the implant's condition and the surrounding tissues. Irregular strain patterns might signal problems like implant loosening, wear, or bone resorption. Furthermore, this monitoring technique assists in customizing rehabilitation programs and recommending activities tailored to individual strain levels. Consequently, such an approach improves recovery outcomes and minimizes associated risks.

To tackle this concern, incorporating implants embedded with sensors for real-time strain monitoring proves beneficial in hip implant surgeries. Embedding biodegradable sensors alongside the implant stem enables the tracking of strain variations, potentially aligning with beneficial bone growth characteristics. Understanding the optimal strain conducive to promoting bone cell growth around the hip implant is critical for rehabilitation. This understanding significantly contributes to the post-surgery recovery process, ensuring effective bone integration.

1.5. Objective of the project

The objective of the project is to design, fabricate and characterize a passive wireless sensor for sensing strain on hip implants for early failure detection.
Key criteria for the design of the strain sensor include:

- the selection of a sensing method adapted to the requested strain sensing range
- a design allowing for wireless power supply and data transmission
- the selection of biocompatible materials to fabricate the sensor, with easy integration into the hip implant
- the sensor must be made entirely from biodegradable materials, including the electrical circuits for sensing and passive wireless transmission of energy and data.

Based on the literature review conducted, it became evident that various criteria were necessary. Each of the criteria is described in brief below.

- Selection of the sensing method and sensing strain range:
  The principal objective is to develop and fabricate a passive wireless sensor capable of detecting strains ranging from 0.5 to 10%, intended for integration into hip implants within the human body [22]. The selection of the sensor's operational range for strain detection aligns with the anticipated deformations associated with potential implant failure.
- Wireless power supply and data transmission:
  Wireless communication is indispensable for telemetry systems integrated into deeply implanted orthopedic implants to avoid the issues such as pain, discomfort, and infection

risks typically linked with wired communication systems [23]. In this context, a passive and wireless system is chosen to collect data from the sensor regarding anticipated deformations.

- Biocompatibility specifications:
  Incorporating sensing systems within implants holds potential benefits. However, it is important to guarantee that these systems neither hinder the implant's regular function nor trigger unfavorable biological reactions. This necessitates miniaturizing components, meticulous material selection, and employing suitable encapsulation methods for the sensing systems [24].
- Biodegradability:
  Developing a biodegradable strain sensor for a hip implant entails specific considerations due to the criticality of its application. The sensor necessitates the capacity to deliver continuous and precise strain measurements throughout its intended lifespan within the hip implant. The sensor's material should gradually degrade over time, ideally reaching complete degradation within a year after the critical phase of the implant's support concludes.

By combining innovative material selection with appropriate biodegradable and biocompatible properties, mechanical suitability, and wireless operability, the project aspires to pave the way for a novel and responsive strain sensor, catering specifically to hip implant applications in the field of biomedical engineering.

1.6. Structure of the thesis

To maintain a structured progression in this project, the subsequent steps were followed.

- In Chapter 1, a concise review and analysis of existing literature were conducted to comprehend various topics, concepts, and the current state-of-the-art knowledge relevant to the project. This review facilitated the identification of gaps in knowledge, contributing to the formulation of specific objectives outlined in Section 1.5.
- In Chapter 2, a sensor was designed in accordance with the predefined objectives.
- Following the finalization of the sensor design in Chapter 2, Chapter 3 centered on the fabrication process within a controlled cleanroom environment, adhering to the developed protocol specific to this sensor.
- In Chapter 4, the sensor underwent modeling and simulation using Computer Simulation Technology (CST) Studio Suite to comprehensively assess its functionality and verify its alignment with the established project objectives.
- Subsequently, the fabricated sensor underwent characterization utilizing an antenna to observe changes in resonance concerning variations in strain.

2

Sensor Design

Strain sensors measure the deformation or strain experienced by an object when exposed to external forces or pressure. They hold significance in diverse medical applications by assessing mechanical deformation or strain within biological tissues or medical devices. Capacitive sensors consist of two conductive materials separated by a dielectric layer, enabling the monitoring of capacitance alterations induced by mechanical deformation.

2.1. Implantable strain sensors: Current technologies

Implantable strain sensors are specialized devices engineered to quantify mechanical deformation or strain occurring within the human body. They hold paramount importance across diverse biomedical applications, offering real-time insights into the mechanical forces endured by tissues, organs, or implants.

2.1.1. State-of-the-art implantable strain sensors

The following section outlines several state-of-the-art technologies related to implantable strain sensors, accompanied by a summary table for reference (Table 2.1).

R. Sun et al. (2019) introduced a stretchable piezoelectric sensor employing kirigami patterns for self-powered, wireless health monitoring of physiological signals and body motions. This sensor's applications in cardiac monitoring and wearable body tracking highlights its potential for various biomedical uses. Their work improves the electrical performance and stretchability of piezoelectric sensors through an innovative intersegment electrode pattern. It demonstrates the sensor's utility in noninvasive cardiac monitoring and wearable body tracking by integrating the Near Field Communication (NFC) technology for wireless communication of strain information. Their results include the development of a kirigami-based stretchable piezoelectric sensor capable of maintaining mechanical integrity while being stretchable. The sensor's power output was enhanced through a novel electrode pattern, showcasing successful applications in cardiac monitoring and wearable body tracking. Conclusions drawn from the paper emphasize that the kirigami technique simplifies the microfabrication process for creating stretchable sensors. The innovative intersegment electrode design improves both mechanical and electrical performances, while the integration of a miniaturized wireless interface allows

for wireless transmission of sensing data [25].

Xu et al. (2021) provided a review of recent progress in flexible skin-like pressure and strain sensors utilized in health monitoring, emphasizing their design, sensitivity, and applications. Their work showed enhancement in health monitoring through advanced flexible sensors that seamlessly integrate with the human body. These sensors improve the design and functionality of implantable medical devices, focusing on biocompatibility and durability. Furthermore, they drive innovation in human-machine interfaces, virtual reality, and robotics through sensitive and adaptable sensor technology. Addressing challenges in non-contact sensing, particularly in scenarios like pandemics where contactless monitoring is preferred, is another benefit. Additionally, these sensors contribute to developing self-healing electronic materials, prolonging the lifespan and reliability of wearable sensors. They also aid in creating intelligent wearable devices and bionic robots with advanced haptic sensing capabilities. Recent advancements in flexible pressure sensors are delineated, elucidating the structural principles and performance characteristics of the flexible strain sensors. It introduces flexible sensors exhibiting favorable biocompatibility and self-driven properties for potential use in implantable bioelectronics [26].

M. Li et al. (2022) proposed a wireless passive flexible strain sensor utilizing aluminum nitride (AlN) film, incorporating an inductor-capacitor loop (LC loop) to improve sensing performance and a structured design optimized for maximum efficiency. This sensor showcases high resolution and sensitivity to micro-strain, suitable for preventing faults and monitoring conditions in mechanical systems. The sensor's compact size (less than 5mm in size) and high resolution enable the detection of micro-strains, aiding in early fault detection. Key findings include an increase in the sensor's resonant frequency from 43.7089 to 43.735 MHz within a strain range of 0-3000 $\mu\epsilon$. It achieved a high strain resolution of 20 $\mu\epsilon$. This sensor's potential applications in condition monitoring and non-destructive evaluation contribute to enhancing engineering safety and preventing failures [27].

Lamanna et al. (2020) introduced a flexible Surface Acoustic Wave (SAW) device based on aluminum nitride (AlN) on a polymeric substrate, showcasing its potential for wireless strain sensing in Internet of Things (IoT) and wearable sensors. It offers a solution to the scarcity of high-performance passive-wireless devices in compliant electronics. The results indicate two resonant modes around 190 MHz and 500 MHz for Rayleigh and Lamb wave propagation, respectively. The study observed a decrease in resonance frequency under tensile strain and a slight increase under compressive strain. The calculated strain responsivity was found to be 0.577 kHz/$\mu\epsilon$ for Rayleigh waves and 1.156 kHz/με for Lamb waves. Additionally, the Limit of Strain Detection (LoSD) was determined to be 4.29E-04 ϵ for Rayleigh waves and 1.81E-04 ϵ for Lamb waves. Although the devices maintained performance under bending conditions, in-band loss and impedance mismatch were observed, indicating areas for potential improvement in future iterations [28].

Jiang et al. (2020) introduced a wireless, passive strain sensing technology utilizing ultrasound imaging of a ZnO nanoparticle-embedded hydrogel for monitoring physiological functions. The hydrogel exhibits high stretchability, optimal mechanical properties, and biocompatibility suitable for diverse body-wide applications. The ZnO nanoparticle-embedded hydrogel,

termed “ZnO-gel” demonstrates the hydrogel’s enhanced elasticity and strength, highlighting the optimal ZnO-to-gel ratio for clear ultrasound imaging and superior stretchability. It provides a solution for remote monitoring of physiological functions by adjusting mechanical properties and nanoparticle concentration addressing limitations of wired connections and onboard batteries in implantable sensors while offering a safer and more stable alternative. The mechanical analysis revealed an optimal ZnO nanoparticle filler ratio of 10% w/w, increasing the hydrogel’s stretchability to 260%. Higher ZnO filler ratios did not significantly affect mechanical strength or elasticity. Biocompatibility tests with fibroblasts indicated no acute toxicity, suggesting the hydrogel’s suitability for physiological applications. Practical implications include enabling wireless and passive monitoring of physiological strains in the body using ultrasound imaging, potential applications in implantable strain sensing for monitoring biological tissue mechanical properties, and offering a biocompatible sensor adjustable for specific applications by tuning nanoparticle concentration. This innovation holds promise for developing new medical devices facilitating real-time, non-invasive monitoring of tissue health and function [29].

Stauffer et al. (2018) introduced a soft electronic strain sensor featuring chipless wireless readout, specifically designed for real-time monitoring of bladder volume. The key contributions include the introduction of a flexible conductor utilizing gold-coated titanium dioxide nanowire layers for applications involving high strain. Additionally, an implantable passive RLC (resistor-inductor-capacitor) circuit equipped with a wireless readout system was developed for comprehensive tissue deformation monitoring. The feasibility of this sensor for continuous, wireless strain monitoring of tissues and organs *in vivo* was demonstrated through *ex vivo* experiments. Their results showcase the successful development of a soft electronic strain sensor integrated with a chipless wireless readout system, tailored for real-time bladder volume monitoring. This sensor system incorporates an implantable RLC circuit featuring a stretchable capacitor, allowing wireless resonance frequency readout. Continuous wireless readout was achieved during 50% strain cycles. The sensor employs Au-TiO_2 nanowire tracks for the stretchable capacitor, which are read by an Arduino-based network analyzer. The practical implications of this innovation are substantial. It enables the continuous and wireless monitoring of tissue and organ strain in real-time, potentially enhancing patient care significantly. Furthermore, it provides a non-invasive method for estimating bladder volume, offering potential benefits in urology and for patients with bladder dysfunction. The sensor’s biocompatibility and passive nature simplify regulatory and safety considerations, making it more feasible for medical use [30].

Another article introduces a wireless, suturable fiber strain-sensing system designed for real-time monitoring of physiological strains in orthopedic applications. This innovative system features a fiber-based passive RLC circuit sensor capable of measuring minute tensile strains on connective tissues, addressing the need for continuous biomechanical signal monitoring. Additionally, the development of a fiber-based passive RLC circuit, integrating a capacitive fiber strain sensor, enables wireless measurement of tiny tensile strains on connective tissue. The establishment of a low-sensitivity initial strain range acts as a buffer during the suturing process, optimizing the practical operation of the fiber strain sensor. The results showcase the successful development of a wireless fiber strain-sensing system for real-time physiological strain monitoring in orthopedic applications. The fiber-based passive RLC circuit sensor ef-

fectively measures minute tensile strains wirelessly. It demonstrated high sensitivity and low noise in detecting tiny tensile strains, achieving a main sensitivity of approximately 12 in the sensing strain range of 15–27.5%. Defining a buffer strain range ensures practical sensor operation by accommodating the initial strain from the suturing process.Practical implications include enabling real-time monitoring of physiological strains, thereby improving orthopedic treatment outcomes. The wireless, suturable design simplifies integration with the body and surgical procedures, while providing high sensitivity and low noise in strain detection, thereby enhancing diagnostic precision [31].

S. Wang et al. (2023) introduced a MXene-based piezoresistive sensor featuring villus-like microstructures, enhancing sensitivity and broadening the detection range. Enabled by a deep-learning algorithm, this sensor accurately captures intricate human movements. Key contributions include the introduction of a bioinspired MXene-based piezoresistive sensor with villus-like microstructures to enhance sensitivity (up to 461 kPa^{-1}) and detection range. A two-stage amplification effect was developed to overcome rapid saturation and low sensitivity in piezoresistive devices. Furthermore, an intermittent architecture resembling human sweat hairs was implemented, enhancing device compressibility and performance. Their results demonstrate a high sensitivity of 461 kPa^{-1} for the MXene-based piezoresistive sensor. The pressure detection range extends up to 311 kPa, significantly surpassing sensors with homogeneous microstructures. Using deep-learning algorithms, the sensor achieved 99% accuracy in identifying complex human movements. Practical implications encompass the development of highly sensitive wearable bioelectronics for advanced motion capture. The sensor's production using laser marking offers a cost-effective and scalable method for piezoresistive sensor manufacture. Its broad pressure-response range facilitates applications in high-pressure environments. Additionally, it improves the accuracy of human motion pattern recognition, beneficial for healthcare and sports analytics. In healthcare, potential applications involve monitoring patient rehabilitation by capturing precise movement data to assess recovery progress, enhancing prosthetic limb functionality through accurate motion detection and feedback, and preventing injury by identifying incorrect movement patterns in real-time [32].

An integrated graphene strain sensor, highly stretchable, sensitive, and biocompatible, has been developed and coupled with a hydrogel for potential clinical applications. This innovative sensor exhibits exceptional durability and adhesion properties suitable for *in vivo* implantation, enabling measurement of an extensive range of human body motions. With the capacity to measure strains up to 500%, this sensor allows for monitoring and distinguishing nearly all human body movements. The sensor's remarkable stretchability and sensitivity facilitate monitoring a broad spectrum of human motions, encompassing subtle facial expressions to extensive limb movements. Its biocompatibility and successful *in vivo* testing suggest promising potential for tracking internal organ movements in clinical settings. [33].

Overall, the primary limitations associated with many implantable strain sensors lie in their non-biodegradable nature. This characteristic presents challenges concerning their extended presence within the body. The absence of biodegradability may require a subsequent surgical intervention for sensor removal once their intended monitoring function is fulfilled or in the event of malfunction. Such additional surgical procedures for extraction may elevate risks, expenses, and discomfort for the patient.

Sr.no	Sensor type	Materials	Applications	Highlights	Pros	Cons	References
1.	Piezoelectric	Kirigami patterns	Cardiac monitoring, Wearable body tracking	Improved electrical performance, Wireless communication, Stretchability	Self-powered, Wireless capability	Fabrication complexity	Sun et al. (2019)
2.	Flexible Pressure /Strain	Various flexible materials	Health monitoring, Implantable devices, Human-machine interfaces	Enhanced sensitivity, Biocompatibility, Non-contact sensing	Diverse applications, Biocompatible	Limited depth of sensing, Surface-oriented	Xu et al. (2021)
3.	Flexible Strain	Aluminum nitride (AlN) film	Condition monitoring in mechanical systems	High resolution, Micro-strain sensitivity, Wireless transmission	High sensitivity, Compact size	Limited strain range	Li et al. (2022)
4.	Surface Acoustic Wave	Aluminum nitride (AlN)	IoT, Wearable sensors	Wireless strain sensing	Wireless capability, Compliant electronics	In-band loss, Impedance mismatch	Lamanna et al. (2020)
5.	Ultrasound-based	ZnO nanoparticle-embedded hydrogel	Remote physiological monitoring, Implantable sensors	Optimal mechanical properties, Biocompatibility, Wireless monitoring	Remote monitoring, Biocompatible	Limited to specific applications	Jiang et al. (2020)
6.	Electronic	Gold-coated titanium dioxide nanowire layers	Real-time tissue and organ monitoring, Urology	Continuous wireless monitoring, Biocompatibility	Wireless, Real-time monitoring	Implantation challenges	Stauffer et al. (2018)
7.	Fiber-based	Various materials	Orthopedic strain monitoring	Minute strain measurement, Wireless operation	High sensitivity, Real-time monitoring	Suturing process impact	Lee et al. (2021)
8.	Piezoresistive	MXene-based material	Healthcare, Sports analytics	Enhanced sensitivity, Broad detection range	High accuracy, Cost-effective	Limited range	Wang et al. (2023)
9.	Graphene-based	Graphene, Hydrogel	Clinical applications, Internal organ monitoring	Exceptional durability, Biocompatibility, *In vivo* implantation	Extensive motion monitoring, Biocompatible	Limited specificity	Cai et al. (2019)

Table 2.1: Summary of the mentioned implantable strain sensors

2.1.2. State-of-the-art implantable biodegradable strain sensors

The following comprises several state-of-the-art technologies within the domain of biodegradable implantable strain sensors, accompanied by a subsequent summary table for reference (Table 2.2).

Implantable biodegradable strain sensors represent an innovative intersection of biodegradable materials and sensing technology. These sensors are designed to measure mechanical strain and offer the advantage of degrading over time, thus eliminating the need for surgical removal post-use.

Salvatore et al. (2017) introduced biodegradable and highly deformable temperature sensors tailored for IoT applications, exhibiting rapid response and stable performance even under mechanical stress. Their key contributions include the introduction of biodegradable resistive temperature sensors crafted from materials like magnesium, silicon dioxide, nitride, and Ecoflex. Achieving a swift sensor response time of 10 ms was made possible through ultra-thin Ecoflex encapsulation. Their results demonstrate the development of fully biodegradable temperature sensors capable of enduring high mechanical deformation. These sensors maintain stable operation with less than 0.7% resistance variation under mechanical stress. Their study showcased a rapid response time of 10 ms, ideal for dynamic monitoring applications, and achieved wireless operation with a resolution of 200 mK, enabling remote sensing. The expanded design to sensor arrays enables flow mapping in smart biodegradable systems. Moreover, customized packaging allows controlled dissolution of sensors within a few days when in contact with water. These biodegradable sensors offer post-surgery monitoring capabilities to track healing progress and reduce infection risk [34].

Boutry et al. (2016) introduced a highly sensitive, fully biodegradable sensor designed for measuring deformation and pressure, specifically intended for monitoring tendon repair post-surgery. Sensor sensitivity is highlighted by its capability to detect strain as low as 0.4% with a signal-to-noise ratio (SNR) of 2.1, indicating superior sensitivity above the detection limit. The sensor exhibits a relative capacitance change of 50 for a 15% applied strain. The key contributions include the introduction of a fully biodegradable sensor capable of measuring both deformation and pressure for orthopedic applications. Significant improvement in sensitivity was achieved by employing a microstructured dielectric layer in the sensor design. The study demonstrated the sensor's ability to monitor tendon repair post-surgery with minimal hysteresis and rapid response times. Their results indicate the development of a highly sensitive, entirely biodegradable sensor for measuring deformation and pressure in orthopedic applications. Stable sensor performance was maintained after thousands of cycles for both strain and pressure measurements. The sensor exhibited sensitivity for strain as low as 0.4% and for pressure as small as 12 Pa. Long-term response validation revealed stable readings over 10,000 cycles for strain and 1,000 cycles for pressure.The sensor's biodegradability ensured safe absorption by the body after fulfilling its monitoring role, thus eliminating the necessity for a second surgery for removal. Its high sensitivity allows for precise monitoring of tendon repair, contributing to personalized patient care and potentially enhancing recovery outcomes [35].

A pressure and strain sensor designed for orthopedic applications was composed of two biodegradable elastomers, namely poly(glycerol sebacate) (PGS) and poly(octamethylene maleate (anhydride) citrate) (POMaC). The developed sensor is implantable within the body to monitor pressure and strain, specifically envisioned for applications in tendon repair. To evaluate its performance, the sensor underwent assessment in real-time both within living organisms (*in vivo*) and in a controlled environment (*in vitro*) using a rat model. The *in vivo* study demonstrated the sensor's functionality for over two weeks, showing consistent performance while gradually degrading over time [36].

R. Yin et al. (2020) pioneered a flexible, biodegradable Ag nanowire/cellulose nanofibril (AgNW/CNF) hybrid nanopaper for strain and temperature sensing, utilizing solution blending and vacuum filtration techniques. The development of this "green" AgNW/CNF hybrid nanopaper is aimed at crafting flexible, biodegradable sensors. The study designed two types of strain sensors with exceptional sensitivity, stability, and durability, potentially applicable in human motion monitoring and physiological signal detection. Additionally, a comprehensive analysis of the hybrid nanopaper's morphology, structure, mechanical properties, and multiple sensing capabilities was systematically conducted. The research also demonstrated the hybrid nanopaper's consistent and reproducible negative temperature sensing behavior. The CNF and AgNW/CNF hybrid nanopapers showcased remarkable flexibility and bendability, with the hybrid displaying a tightly stacked structure.It offers a solution for fabricating sensors with ultralow detection limits, suitable for precise strain and temperature monitoring. The research provides guidelines for constructing sensors adept at detecting human motion [37].

An ultra stretchable, self-powered organogel/silicone fiber-helical sensor (OFS-TENG) designed for real-time, implantable monitoring of ligament strain, showcasing rapid preparation, high stretchability, and stability was developed. This sensor enables the diagnosis of muscle and ligament injuries. The sensor's sensitivity and stability were demonstrated, offering

a novel platform for self-powered sensors and health monitoring applications. Additionally, systematic *ex vivo* and *in vivo* tests confirmed the OFS-TENG's biocompatibility. The ultra-stretchable OFS-TENG was developed specifically for implantable ligament strain monitoring, showcasing impressive performance and stability, maintaining nearly 90% of its original electrical output over six months. *In vivo* tests in rabbits exhibited good biocompatibility and a stable sensor response after four weeks of implantation. Mechanical behavior analysis revealed that the organogel's Young's modulus increased with strain rates, signifying elastic deformation. Practical implications include facilitating real-time, power-free monitoring of muscle and ligament strain, aiding in injury diagnosis and rehabilitation. The sensor provides a solution for implantable sensors, overcoming limitations such as the need for external power and poor flexibility. Integration with wireless technology could yield a smart, self-powered, and wireless sensing system [38].

Hanif et al. (2021) introduced a biodegradable, biocompatible, and stretchable composite microfiber composed of poly(glycerol sebacate) (PGS) and polyvinyl alcohol (PVA), suitable for transient stretchable electronics. A strain sensor employing gold nanoparticles (AuNPs) demonstrated stable performance under dynamic stretching, effectively monitoring diverse human movements such as finger, knee, and esophagus activities. The study highlighted the rubber-like elasticity of PGS, rendering it suitable for dynamic environments and wearable electronics placed on the body. The results showcased the successful preparation of composite microfibers using varying mass ratios of PGS and PVA, exhibiting improved mechanical properties. The strain sensor developed using this composite microfiber and AuNPs displayed a stable current response under 30% strain, enabling the monitoring of various human movements. Practical implications of this composite microfiber lie in its utilization within biodegradable and stretchable electronics, contributing to reduced environmental impact. Moreover, its potential applications extend to wearable devices that conform to body movements, while the microfiber-based strain sensor holds promise for monitoring physiological activities, particularly in healthcare applications [39].

Boutry et al. (2019) introduced a biodegradable, flexible arterial-pulse sensor designed for wireless blood flow monitoring after surgical procedures, negating the necessity for device removal. The sensor's effectiveness was demonstrated both *in vitro* using an artificial artery model and *in vivo* in a rat model. Additionally, the study addresses the challenge of monitoring microvascular anastomoses by designing the sensor to work on small blood vessels. Moreover, it provides a solution to eliminate the need for postoperative extraction surgery of the monitoring device. The results demonstrated successful *in vitro* pulse monitoring with a custom-made artificial artery model and excellent biocompatibility and pulse monitoring function *in vivo* in a rat model. The sensor's wireless operation was enabled through radio-frequency coupling, allowing for remote monitoring. Importantly, the device, composed entirely of biodegradable materials like magnesium (Mg), poly(glycerol sebacate), (PGS)poly(octamethylene maleate (anhydride) citrate) (POMaC) which naturally resorbs after several months, eliminating the requirement for surgical removal. Practical implications encompass enhanced postoperative blood flow monitoring, potentially reducing complications and repeat interventions. Elimination of the need for additional surgery to remove the monitoring device due to its biodegradable nature is a significant advantage. The continuous, wireless monitoring of vascular patency after patient discharge improves long-term care and might contribute to reducing healthcare costs

by preventing graft failure and tissue loss through early detection [40].

The development of biodegradable sensors is hindered by the limited availability of appropriate materials for semiconductors, conductors, dielectrics, and protective encapsulation. Differing degradation rates among these materials can significantly influence the sensor's operational durability, necessitating effective encapsulation strategies to ensure stability. However, the selection of suitable materials for sensor encapsulation is complex due to concerns related to swelling and water permeation within biodegradable materials and polymers. Additionally, the fabrication of biodegradable sensors demands the utilization of gentle and adaptable techniques, such as soft lithography, which are frequently characterized by high costs and time-consuming processes [41].
In summary, the limitations associated with the majority of the mentioned implantable biodegradable strain sensors predominantly involve the characteristics of biodegradable materials. These materials might exhibit diminished mechanical strength compared to non-biodegradable alternatives, which could potentially influence the operational efficiency of the sensor. Additionally, regulating the biodegradation rate presents a considerable challenge, as sensors may undergo degradation at either an accelerated or decelerated pace, thereby affecting functionality or causing unforeseeable degradation processes within the body. Furthermore, the complexity of manufacturing biodegradable sensors with consistent properties and performance, while ensuring biocompatibility and controlled degradation, significantly complicates the production process. Attaining a balance among degradation rates, sensor functionality, and biocompatibility stands as a critical factor in advancing the efficacy and dependability of biodegradable strain sensor.

Sr.no	Sensor Type	Materials Used	Applications	Highlights	Pros	Cons	References
1.	Resistive strain/ temperature sensors	Magnesium, silicon dioxide, nitride, Ecoflex	IoT, Post-surgery monitoring	Biodegradable, Rapid response , Stable performance under mechanical stress	Remote sensing, Dissolvable in water	Fabrication complexity	Salvatore et al. (2017)
2.	Strain and pressure sensors	Microstructured dielectric layer	Orthopedic applications - Tendon repair	Highly sensitive , Stable performance	Biodegradable, Minimal hysteresis	Limited to specific medical applications	Boutry et al. (2016)
3.	Pressure and strain sensors	Poly(glycerol sebacate) (PGS), Poly(octamethylene maleate (anhydride) citrate) (POMaC)	Orthopedic applications	Minimum strain detection Low-pressure sensitivity	Long-term stable performance	Limited depth of detection	Boutry et al. (2018)
4.	Strain and temperature sensors	Ag nanowire/cellulose nanofibril (AgNW/CNF) hybrid	Human motion monitoring, Physiological signal detection	Exceptional sensitivity, Flexible & bendable	Ultralow detection limits	Limited specificity	R. Yin et al. (2020)
5.	Ligament strain sensor	Organogel/silicone fiber-helical sensor (OFS-TENG)	Implantable ligament strain monitoring	Self-powered, stability	Real-time monitoring, Biocompatible	Implantation challenges	Sheng et al. (2022)
6.	Composite microfiber strain sensor	Poly(glycerol sebacate) (PGS), Polyvinyl alcohol (PVA), Gold nanoparticles (AuNPs)	Transient stretchable electronics, Wearable devices	Stable response Suitable for dynamic environments	Biodegradable, Suitable for body-conforming devices	Limited strain range	Hanif et al. (2021)
7.	Arterial-pulse sensor	Magnesium (Mg), Poly(glycerol sebacate) (PGS), Poly(octamethylene maleate (anhydride) citrate) (POMaC)	Wireless blood flow monitoring	*In vitro* and *in vivo* pulse monitoring, Biodegradable	Wireless operation, Biocompatible	Limited to specific vascular application	Boutry et al. (2019)

Table 2.2: Summary of the mentioned implantable biodegradable strain sensors

2.2. Choice of design for the Device

To enhance the comprehension of the implantable biodegradable strain sensor for this project, an in-depth analysis and examination of the design for an implantable strain sensor were conducted.

The strain sensor's design in this study draws inspiration from the research conducted by M. Li et al. (2022). Li et al. proposed a wireless passive flexible strain sensor utilizing an aluminum nitride (AlN) film. The sensor design incorporates a thin layer of aluminum nitride (AlN) film deposited onto copper electrodes, leveraging its favorable piezoelectric properties and chemical stability. Notably, the sensor demonstrates a high strain resolution (strain range: 0–3000 $\mu\epsilon$, resolution: 20 $\mu\epsilon$) and is well-suited for monitoring mechanical systems operating at low a frequency (43.70 MHz) [27].

2.3. Biodegradable materials selection

Biodegradable materials tend to degrade over time, gradually breaking down and to be absorbed by the body. They must be biocompatible to reduce the likelihood of triggering significant foreign body responses or any adverse reactions when in contact with the body, thereby decreasing the chances of infection or discomfort commonly associated with implantation [42]. Biodegradable materials for sensors in the case of hip implant applications enables customization to match the required lifespan [43]. Various biomaterials commonly used are summarized in Table 2.3. Sensors fabricated using biodegradable materials can eliminate the necessity for a second surgery to remove the implant since they degrade within the body, thereby reducing patient discomfort and the risks associated with second surgery [44].

	Material	Sensor component	Advantages	Limitations
1	Magnesium (Mg)	Wires, pads, and electrodes Coils and antennas for wireless transmission Transducer conductive thin film	Easy processing Essential nutrient High energy density Long shelf-life	Fast dissolution kinetics, tend to crack and fragment Degradation products can be toxic in high amounts
2	Iron (Fe)	Adhesion layer Cathode for batteries	Essential nutrient Easy processing Good mechanical properties Homogeneous dissolution with no fragmentation	Fe toxicity could lead to gastrointestinal and liver damage and shock Ferromagnetism can hamper Magnetic resonance image Bad choice for LC resonators due to low Q factor, skin depth, and high resistivity in high frequencies due to skin effect Degradation rate too low for complete removal after 6–24 months
3	Zinc (Zn)	Transducer component (in combination with Fe)	Reasonable electrical characteristics for high Q elements	Slow degradation
4	Molybdenum (Mo)	Electronics component	High strength and Youngs modulus Compatible with magnetic resonance imaging (MRI)	Calcium presence in simulated body fluid slow considerable the Mo degradation Degradation *in vivo* models has not been studied in detail
5	Polylactide (PLA) and its derivates	Packaging Wires electrical insulation Seal glue (in combination with acetone and chloroform)	Soft, mechanical and degradation can be tuned Water and electrical proof Easy processing	Hydrophilic behavior could lead to swelling and water infiltration producing premature failure
6	Poly[octamethylene maleate (anhydride) citrate] (POMaC)	Packing		
7	Polyvinyl alcohol (PVA)	Adhesive layer		
8	Poly(glycerol sebacate) (PGS)	dielectric layer		

Table 2.3: Summary of biodegradable materials that can be used in sensing systems.

Molybdenum demonstrates favorable biocompatibility, interacting well with biological systems, thereby mitigating the likelihood of adverse reactions or tissue rejection when employed in medical implants or sensors. With outstanding mechanical properties, molybdenum can be tailored to showcase controlled degradation features, ensuring the gradual and predictable breakdown of the sensor within the body over time in a secure and anticipated manner. Its versatility extends to various fabrication techniques, enabling the creation of complex sensor designs with ease.

Molybdenum has been selected as the metal of choice for fabricating the strain sensor owing to its favorable mechanical properties (Young's modulus value being 315 GPa), biodegradability, and biocompatibility summarized in Table 2.3 [45].

2.4. Theoretical background - Interdigical capacitive strain sensor

This project uses an interdigital capacitive strain [46] sensor due to its capability of detecting small stain changes causing changes in capacitance [47] .
The sensor is known for exhibiting a high sensitivity, which is beneficial for hip implant applications where monitoring small and subtle changes is crucial, which helps give information on the physiological parameters. The capacitor can be designed in a very small scale depending on the application and can be fabricated precisely in the cleanroom [48]. This shows flexibility in the design and fabrication of the said sensor that is ideal for a compact design needed for sensing strain in hip implant applications.
Another important feature of an interdigital capacitive strain sensor is its ability to be integrated with wireless technology that enables real-time data transmission without the need for physical connections [49]. This feature is advantageous in medical applications as it allows for continuous monitoring without hindering the patient's mobility or comfort. In this way the sensor can offer good reliability in its measurements, hence providing accurate and consistent information and helping the care providers to make an informed healthcare decision [46].

Capacitive strain sensors are frequently utilized detectors that utilize alterations in capacitance to indicate changes in stress [49]. These sensors can detect various physiological signals within the human body. Despite the influence of the fringe effect, the capacitance between the capacitor's two plates is

$$C = \frac{\epsilon_0 \epsilon_r A}{d}$$

where,
ϵ_0 = permittivity of free space,
ϵ_r = relative permittivity of the dielectric material,
A = area of the plate,
d = distance between the plates

The theoretical equation for calculating the interdigital capacitance is,

$$C = (N-1)\,\epsilon l \left[\frac{K(\xi)}{K(\xi)} + \frac{h}{g}\right]$$

where,
N = number of interdigits,
ϵ = permitivitty,
h = thickness of the interdigit finger,
l = length of the interdigit,
g = the distance between two intergits (gap).

$K(\xi)$ is known as the complete elliptical where ξ and ξ‘ are,

$$\xi = sin\left(\frac{\pi}{2}\frac{g}{w+g}\right)$$

$$\xi^{'} = \sqrt{1-\xi^2}$$

where w is the width of the interdigits.

It can be observed that the change in permittivity of the interdigital capacitance depends on the finger width ‘w’, finger length ‘l’, interfinger spacing ‘g’ [50].

2.5. Design and sensing: Wireless sensing methods

2.5.1. Theoretical background – LCR resonators

The utilized passive sensor functions based on an LC (inductive-capacitive) circuit that has a strain-sensitive capacitor as its core sensing element and an inductor coil. This together forms an LC circuit [51]. The changes in deformation alter the sensor’s resonant frequency, enabling wireless data transmission [52]. An external antenna is employed for observing the resonance frequency and bandwidth changes.

When a passive sensor has an LC circuit, it means that changes in the surrounding environment affect the inductance, capacitance, or both, thereby altering the resonance frequency. Here, the capacitive sensor changes its capacitance due to strain which leads to the change in resonance frequency. By understanding and measuring the changes in resonant frequency, the changes in strain can be determined [49]. The resonant frequent is represented as,

$$f = \frac{1}{2\pi\sqrt{LC}}$$

where,
f = resonant frequency,
L = inductance of the sensor,
C = capacitance of the sensor.

The LC circuit facilitates wireless communication by frequency in response to strain. This wireless capability eliminates the need for physical connections for communication between the sensor and the antenna system [53]. Due to the passive nature, the sensor can function

wirelessly without the need for an internal power supply [49]. This eliminates the need for periodic battery replacements.

The frequency response of an LC circuit can be tailored to the specific requirements depending on the application. The customization allows for the optimization of the sensor's performance, making it more suitable for monitoring the unique strain patterns.
These circuits can be tailored to compact sizes, allowing the creation of small strain sensors ideal for embedding into hip implants. This design ensures the sensors fit within the patient's physical dimensions, ultimately reducing any discomfort experienced by the patient. LC circuits can exhibit high sensitivity to changes in strain and therefore allows for accurate measurements of mechanical stress or deformation [49].

In a system where an antenna interacts with a passive wireless LC (inductive-capacitive) capacitive strain sensor, electromagnetic coupling principles are typically employed for sensing. This sensor contains an LC (inductive-capacitive) circuit that causes changes in the capacitance of the sensor due to strain that can modify the resonance frequency. The LC circuit in the passive sensor is typically designed and tuned to resonate at a specific frequency. When an external antenna generates an electromagnetic field, this field carries information. The LC circuit, when in proximity to this field, is designed to interact with it more effectively at its resonant frequency.
The electromagnetic field emitted by the antenna induces voltage and influences the behavior of the LC circuit in the sensor, enabling the transmission and receiving of wave amplitudes.
The reader device detects these changes/modulations, decodes and interprets the transmitted and received waves amplitudes to understand the strain that is sensed by the passive wireless sensor [54]. Mutual inductance coupling in Figure 2.1 allows for wireless transmission between the antenna and the passive sensor without physical connections.

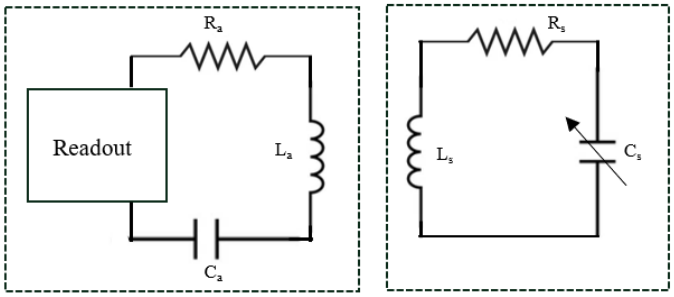

Figure 2.1: Mutual inductance coupling of the sensor where,
L_a, C_a, R_a is the inductance, capacitance and resistance of the antenna respectively and L_s, C_s, R_s is the inductance, capacitance and resistance of the strain sensor [55].

2.5.2. Sensor performance parameters

The capacitive sensor is mainly based on the strain or the deformation of the sensor [56]. The equation of strain being,

$$strain = \frac{\Delta l}{l}$$

where,
Δl = change in dimension of the structure,
l = original dimension of the structure.

Due to the deformation, there is a change in permittivity, causing a change in capacitance. This change in capacitance causes a shift in the resonance frequency.

In applications, the reader shows the change in resonance, which can help us understand the change in strain.

2.5.3. Wireless operation of the strain sensor

A slot antenna is an electromagnetic device that operates by exploiting an aperture or slot in a conductive material, typically a metallic plate, and is predominantly employed in microwave and radio frequency domains. Functioning on the principle of electromagnetic radiation, this antenna utilizes the slot as an opening through which electromagnetic energy is emitted or received. Upon application of a radio frequency (RF) signal, an alternating current is induced, oscillating across the slot. Consequently, this alternating current generates electromagnetic waves that propagate outward from the slot. The slot's dimensions and the material properties of its surroundings dictate the antenna's radiation pattern and overall performance. Slot antennas are extensively utilized across various wireless communication applications, such as Wi-Fi, Bluetooth, and RFID systems. They also serve in radar systems for both signal transmission and reception, owing to their capacity to achieve broad bandwidths and directional radiation [57].

The sensor is used with an external slot antenna placed outside the body [58].
The model is characterized using S11 to analyze the performance of wireless data transfer. The operating frequency from the simulation is approximately 0.4 GHz. Theoretically, the frequency is calculated using

$$f = \frac{1}{2\pi\sqrt{LC}}$$

where,
f = resonant frequency,
L = inductance of the sensor,
C = capacitance of the sensor.

This frequency is expected to change with variations in strain.
To analyze and check if the sensor is capable of operating at a frequency of 400 MHZ and exhibits a strain range of 2-10%, a simulation model was set up on the Computer Simulation Technology (CST) simulation platform.

3

Strain Sensor Fabrication

This chapter presents an extensive explanation of the fabrication procedure employed for the strain sensor. The determination of the sensor's design and dimensions relies on the equation delineated in the previous chapter. Once the structural dimensions are conclusively established, a mask design resembling these dimensions is generated using specialized software (as discussed in Section 3.1). Subsequently, the fabrication process is executed within a controlled cleanroom environment (as outlined in Section 3.2). The sensor was designed using the parameters in Table 3.1 and shown in Figure 4.2.

Determining the requisite capacitance using the aforementioned equations and aligning them based on the desired frequency led to the derivation of the sensor's dimensions.

l	w	g	h	R_1	R_2	N
4.5	0.08	0.08	0.018	26	29	15

Table 3.1: Device Parameters in mm except for N. Here, l is the length of the interdigit, w is the width of the interdigit, g is the gap between the interdigits, R_1 is the internal radius of the inductor coil, R_2 is the external radius of the inductor coil, and N is the number of digits.

3.1. Mask design

Utilizing the dimensions outlined in Table 3.1, the configuration for patterning electrodes was developed using L-Edit software, illustrated in Figure 3.1. L-Edit, a layout editor primarily employed in the creation of integrated circuits (ICs) and layouts, was specifically utilized in this context to design the layout of electrodes necessary for the fabrication of the sensor.

The photomasks served an important role in the photolithography process by delineating the precise patterns that could be replicated onto the wafers. Their accuracy and precision (mentioned in Section 3.2) bore significant importance as they would directly influence the functionality and structural integrity of the fabricated device [59]. Maskless lithography stands as an important technique within semiconductor manufacturing, enabling pattern creation on substrates without reliance on physical masks. This process entails the utilization of a concentrated laser beam or alternative light sources to inscribe patterns directly onto the substrate.

This technique offers versatility in pattern adjustment and facilitates rapid prototyping [60]. Its implementation yields multiple advantages, notably enhanced design flexibility, accelerated prototyping, and decreased expenses linked to mask manufacturing. Noteworthy for its commendable resolution capabilities, maskless lithography facilitates the generation of intricate and precise patterns on substrates, empowering the fabrication of minute features and structures. Furthermore, these methods frequently demonstrate superior alignment and overlay accuracy between layers or patterns on substrates. Such precision plays a crucial role in device fabrication, where optimal alignment significantly impacts functionality. Although maskless lithography presents various advantages, it is not without limitations. Attaining exceedingly high resolutions in maskless lithography systems poses challenges, particularly when scaling up for large-scale manufacturing. While this lithographic method enables the flexibility to generate tailored patterns, its efficiency might diminish when handling highly repetitive or standardized patterns. In Figure 3.1, each labeled structure from ‘a’ to ‘f’ denotes a distinct level of strain: structure ‘a’ signifies 0% strain, ‘b’ signifies 2% strain, ‘c’ signifies 4% strain, ‘d’ signifies 6% strain, ‘e’ signifies 8% strain and ‘f’ signifies 10% strain.

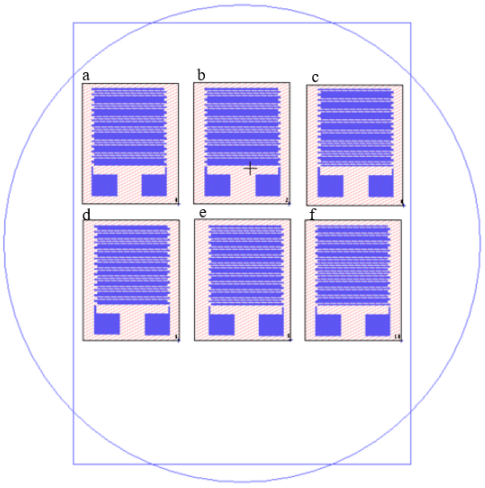

Figure 3.1: Mask design created on L-edit software showing the sensor design ‘a’-‘f’ with varying strain 0-10% respectively utilizing the dimensions outlined in Table 3.1.

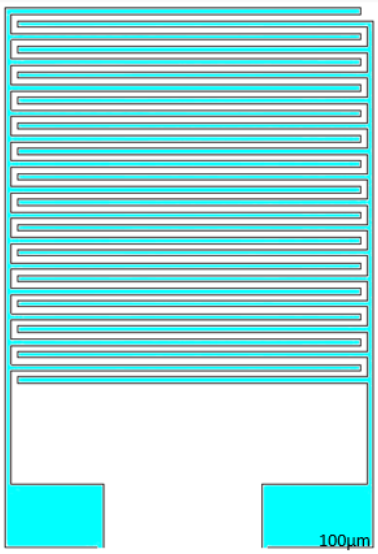

Figure 3.2: Zoomed in image of one of the structures (here 0% strain, corresponding to capacitance = 10.7385 pF) in mask design created on L-edit software showing the sensor design with varying strain 0-10% utilizing the dimensions outlined in Table 3.1.

3.2. Fabrication steps

The fabrication methodology outlined in the study drew initial inspiration from the protocol devised by Salvatore et al. (2017) [34]. However, specific modifications were introduced to tailor the protocol to suit the specific requirements of the sensor for this project. Notably, certain steps involving reactive ion etching and the encapsulation process using Ecoflex/POMaC were not performed. This adaptation was implemented to streamline the initial protocol and expedite structure fabrication, thereby enabling the characterization of the structures within the project's constrained timeframe. Instead, a simplified, alternative fabrication process without the encapsulation was employed to achieve the desired structure for this project.

The original research utilized magnesium (Mg) as the primary material for fabricating the biodegradable sensor. However, challenges arose in implementing Mg within the controlled environments of the EKL and Kavli NanoLab cleanrooms at TU Delft University due to its unavailability. Magnesium is highly reactive, readily forming a protective oxide layer upon exposure to oxygen, hindering adhesion and altering the desired properties of the deposited film. Moreover, magnesium targets used in sputtering are susceptible to degradation, exhibiting tendencies for cracking and defect formation due to their soft and brittle nature. Furthermore, sputtering of magnesium generates thermal energy as a result of its interaction with high-energy ions, leading to localized heating, which is undesirable in this context. Hence, the sputtering of magnesium was deemed unsuitable for use within the cleanroom facilities. Iron (Fe) emerged as an alternative biodegradable metal; however, it is prone to corrosion, particularly in biological environments or when exposed to moisture. Corrosion alters the material's physical characteristics, potentially inducing changes in its resonance properties. These alterations, alongside corrosion-related variations, could introduce noise or interference in the sensor's signals, compromising the accuracy and sensitivity of strain measurements.

Consequently, molybdenum (Mo) was selected as the material of choice for the sensor fabrication process of metal electrodes since it was readily available in the EKL laboratory, providing a viable alternative given the challenges associated with magnesium in this specific research context in terms of the objective of the sensor being biodegradable and biocompatible.

A standard clean Si wafer was taken onto which PMMA (AR-P 672.045,950K,4.5% in Anisole, Allresist) was spin-coated at 3000 rpm for 30 s and baked for 1 min at 180 °C (step 'a'). 2 μm Polyimide (Fujifilm LTC 9305) layer was spin-coated at 5000 rpm for 30 s and initially baked at 100 °C for 200 s and further hard-baked in a KOYO oven at 400 °C for 4-5 h (step 'b').
A bottom encapsulation layer was formed by 100 nm of SiO_2, deposited using PECVD at 120 °C (step 'c'). 250 nm of Mo was deposited at room temperature by magnetron sputtering (step 'd'). To pattern the Mo layer, photoresist AZ ECI 3027 was spin-coated on the wafer and baked at 115°C for 120 s. It was followed by maskless lithography to pattern the electrode design (step 'e'). The upper encapsulation was formed by depositing of 300 nm of Si_3N_4 by applying plasma enhanced chemical vapor deposition (PECVD) at 120 °C (step 'f'). The main fabrications steps 'a' to 'g' are illustrated in Figure 3.3.

2 μm Polyimide (Fujifilm LTC 9305) layer was spin-coated at 5000 rpm for 30 s and initially baked at 100 °C for 200 s and further hard-baked in a KOYO oven at 400 °C for 4-5 h followed by depositing additional 500 nm of SiO_2 by PECVD at 120 °C (step 'g'). This step of depositing additional PI and SiO_2 layers is optional for this project.
Initial sensors in the first generation lacked PI and SiO_2 layers, causing curling upon detachment. Second-generation sensors had these layers deposited on the substrate over the original stack but faced bubble-induced damage on the substrate. Third-generation sensors were fabricated without these layers, focusing on limited duration in acetone bath and careful release onto a glass substrate. Therefore, the step ('g') involving the deposition of PI and SiO_2 layers is regarded as optional for this project due to the observed challenges and issues encountered in the sensor fabrication process associated with these layers across different generations.

The wafer was diced along the pattern of the structure, thereby making the individual pattern separated on a separate die (step 'h' and 'i'). The diced die is illustrated in Figure 3.5. The individual die was placed in 40 °C acetone bath for 4-5 min to dissolve the PMMA layer (step 'j' shown in Figure 3.4). This released the device structure from the Si die (step 'k').

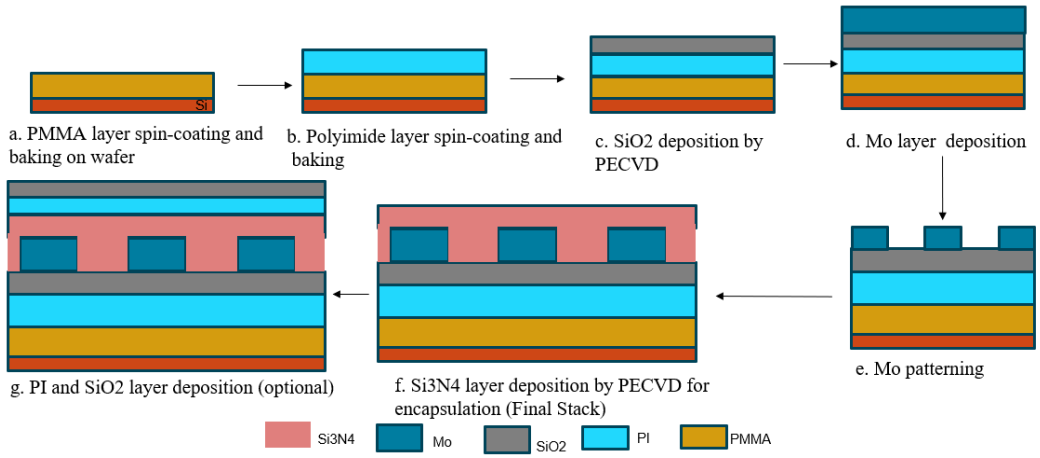

Figure 3.3: Fabrication steps involving the deposition of the materials.

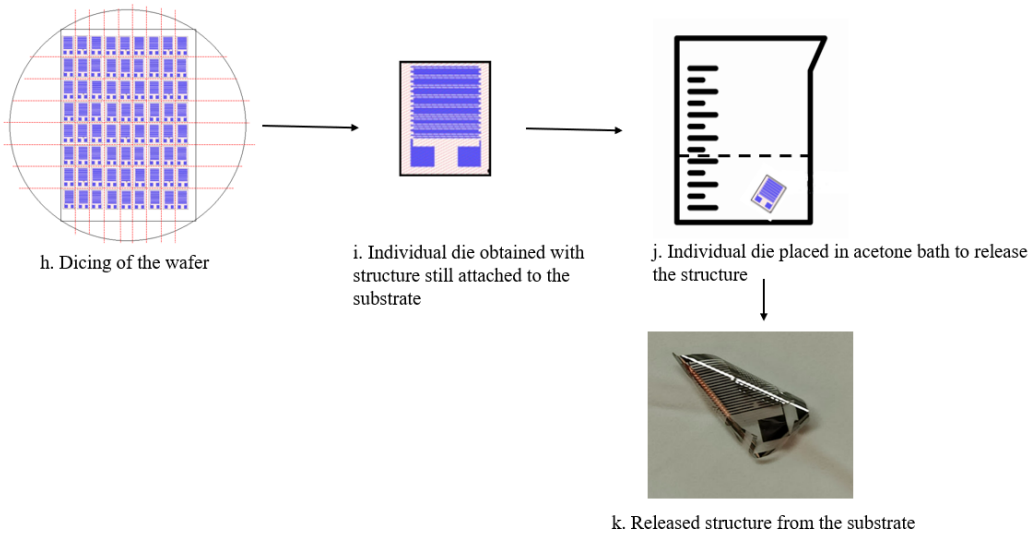

Figure 3.4: Remaining fabrication steps involving dicing of the wafer and releasing the structure from the substrate.

3.2.1. Fabrication process: Procedure and main difficulties encountered

The process began by applying PMMA and PI layers onto a clean wafer surface using Cee Apogee Spin Coater (steps ‘a’ and ‘b’). Next, a base encapsulation layer made of SiO2 was deposited using PECVD via the Oxford PlasmaPro100 ICPECVD tool (step‘c’) on the well-baked PI layer. Following this, a layer of molybdenum metal was deposited at room temperature using Trikon Sigma 204 (step‘d’). A lithography process using the Maskless Aligner MLA 150 defined the electrode design on the wafer (step‘e’). Subsequently, an additional Si3N4 encapsulation layer was deposited using PECVD through the Oxford PlasmaPro100 ICPECVD tool (step‘f’). Dicing the wafer created individual dies, each displaying the designed structure

shown in Figure 3.5. These diced wafers were soaked in warm acetone for 4-5 min to release the delicate structure or potential sensor from the silicon substrate. Every step and tools within the fabrication protocol mentioned in this section was executed at the EKL laboratory, with the exception of the maskless lithography process, which was conducted at the Kavli NanoLab.

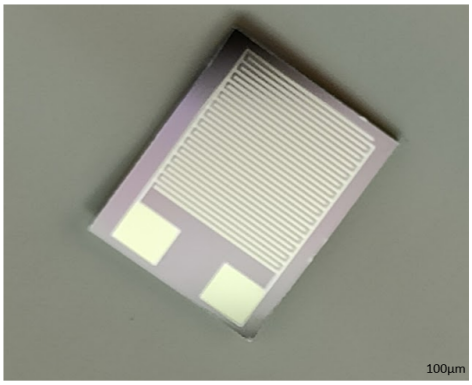

Figure 3.5: Individually diced structures, with the structure attached to the Si wafer

The primary challenge encountered during these procedures arose when attempting to remove the released structure from the acetone bath. Once the structure was detached from the silicon, it exhibited a tendency to curl, shown in Figure 3.6, presenting significant difficulty in restoring it to a flattened state, shown in Figure 3.7.
The observed occurrence may stem from either the stress induced by the Si_3N_4 layer on the metal layer or an extended immersion period in the acetone bath. Initially, during the fabrication process, the structure underwent an acetone bath lasting approximately 10-12 min. Suspecting structural distortion upon detachment from the substrate, the duration of the acetone bath was subsequently reduced to 4-6 min to achieve the structural configuration depicted in Figure 3.9.

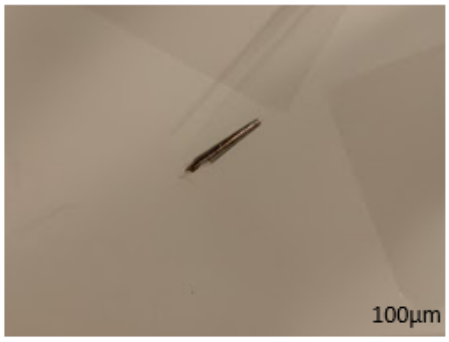

Figure 3.6: Curling of the structure seen after removing from the acetone bath

In an attempt to address this issue, an additional layer of PI was spin-coated and subjected to a high-temperature hard bake (below 400 °C in an oven). This was performed on top of the original stack comprising PMMA, PI, SiO_2, Mo, and Si_3N_4 layers, followed by another layer of

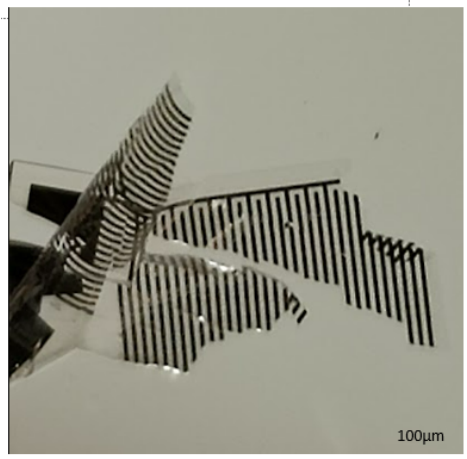

Figure 3.7: Tearing of the structure while attempting to flatten it, destroying the metal lines

SiO_2. The intention behind this step was to enhance the structural robustness of the assembly subsequent to its detachment from the silicon substrate. However, following the hard bake of the PI layer at temperatures below 400 °C, the appearance of bubbles was observed on the surface, shown in Figure 3.8. This occurrence rendered the structure unusable, possibly resulting from the outgassing of the oxide layers at elevated temperatures. The decision to refrain from depositing the additional PI and SiO_2 layers was made due to the presence of bubbles formed on the substrate.
The initial sensors, constituting the first generation, lacked the presence of PI and SiO_2 layers. Consequently, upon detachment from the substrate, these sensors exhibited a tendency to curl up, posing significant challenges in the flattening process without jeopardizing the integrity of the metal lines. Subsequent improvements in the second generation involved the deposition of PI and SiO_2 layers in alignment with the original reference paper [34]. Nevertheless, during the hard bake of these layers, the occurrence of bubbles on the substrate led to damage in the second generation sensors. Advancements in the third generation entailed forgoing the deposition of PI and SiO_2 layers. Instead, a meticulous approach was adopted, limiting the duration of the acetone bath and exercising utmost care during the release of the structure onto a glass substrate.

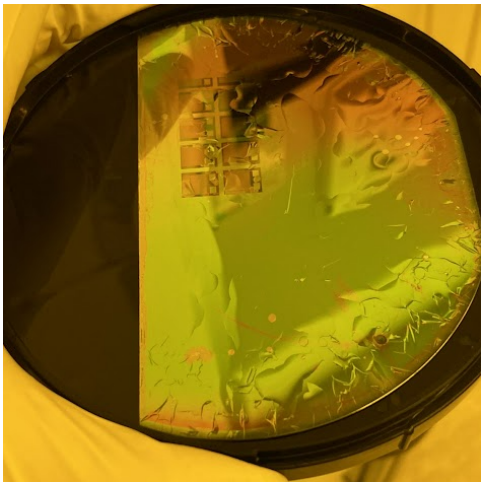

Figure 3.8: Bubbles on the wafer after hard-bake of the PI layer

An alternative method employed to flatten the structure involved sandwiching the structure (with the original stack of materials: PMMA, PI, SiO_2, Mo, and Si_3N_4 layers) between two exceedingly thin glass substrates. This approach effectively preserved the integrity of the released structure (including the preserved structure of the metal lines) while aiding in its flattening.

3.3. Final Structure

The final biodegradable strain sensor, illustrated in Figure 3.9 and featuring dimensions specified in Table 3.1 (without the inductor loop), was manufactured within a cleanroom environment utilizing the fabrication methodology outlined in Chapter 2. Six distinct structures, each denoting a different strain (changing the gap distance between the interdigits), as depicted in Figure 3.1, were fabricated using the fabrication steps mentioned in this section.
The magnified view of the depicted final strain sensor in Figure 3.10 illustrates the integrity of the metal lines and confirms adherence to the specified dimensions outlined in the mask (Table 3.1) during the fabrication process.

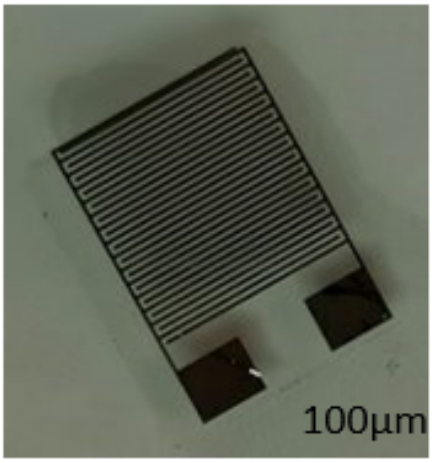

Figure 3.9: Final strain sensor fabricated in the cleanroom.

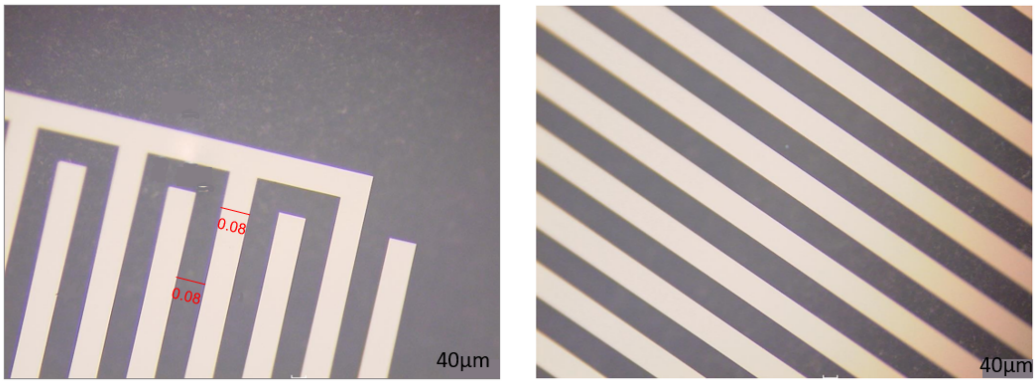

Figure 3.10: An enlarged image of the completed structure (showing 0% strain), produced within the cleanroom environment, highlights various regions on the sensor, demonstrating the integrity and continuity of the metal lines across the structure (the metal lines are shown in light shade).

The fabricated sensor(s) (depicting different strains) was subsequently employed for characterization in conjunction with an antenna, as elaborated in the forthcoming chapters.

4

Simulations and Characterization

4.1. CST simulation platform

To evaluate the functional performance of the constructed sensor operating at a frequency of 400 MHz, a model integrating both the sensor and antenna was devised for analytical assessment. In order to simulate the designated sensor with parameters delineated in Table 3.1, CST Studio Suite was utilized.

4.1.1. Simulations on CST

To evaluate the operational performance of the developed sensor operating at a frequency of 400 MHz, a comprehensive model integrating both the sensor and antenna was established to conduct thorough analysis and assessment.

To model the specified sensor according to the parameters outlined in Table 3.1, the CST Studio Suite is employed for simulation purposes. Analyzing the shifts in resonance frequency aids in determining the sensitivity of the sensor.

The CST simulation was employed to observe alterations in resonance frequency by integrating a custom-designed antenna. This facilitated the monitoring of capacitance variations induced by deformations in the sensor caused by strain. Through the utilization of the Time Domain Solver, the simulation showcased its capability to explore an extensive frequency spectrum. This inclusive analysis spanned both low and high-frequency electromagnetic effects seamlessly, eliminating the need to transition between diverse solvers or methodologies [61].

The “Time Solver” function represents a computational methodology employed for the analysis of electromagnetic fields across a temporal spectrum. It computes the dynamic changes of these fields over time, considering prescribed boundary conditions, material characteristics, and excitation sources. Following the simulation, the Time Solver facilitates the visualization of time-evolving electromagnetic field distributions. It also provides insights into variables such as electric and magnetic field strengths, currents, voltages, and other pertinent parameters throughout the duration of the simulation.

4.1.2. Strain sensor modelling

The design and modelling of the sensor described in this project were based on the following specified conditions.

- Geometry: The sensor's design shown in Figure 4.1 adhered to the specifications outlined in Table 3.1. The entirety of the sensor system, illustrated in Figure 4.3, is employed within simulation setups.

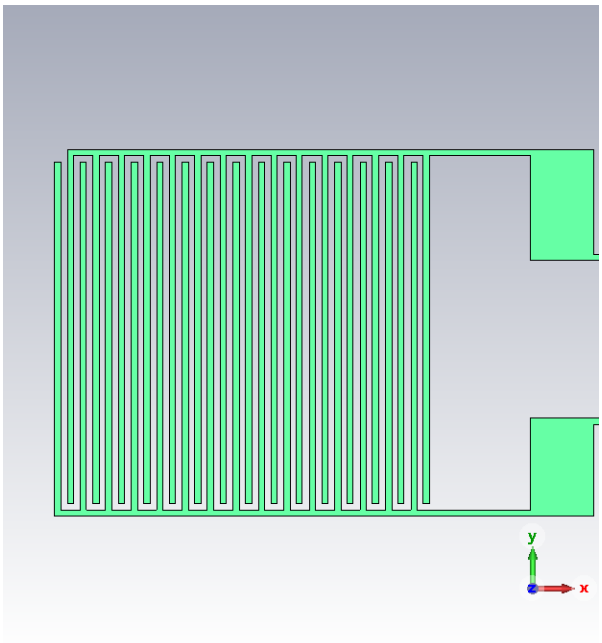

Figure 4.1: Sensor modelled in CST

Figure 4.2: Zoomed in image (90° rotated from the above image) of the sensor modelled in CST showing the length 'l', width 'w' and gap 'g' of the interdigits that is mentioned in Table 3.1

- Components: Each element, encompassing the sensor's constituent materials, antenna structure, and biological tissues, underwent individual specification. Instances where materials were absent from the CST library necessitated a manual integration process. This involved incorporating the properties of these materials into the software's library, thereby enabling their inclusion in the simulation. Detailed descriptions of the various materials utilized are outlined in Table 4.1.

- Mesh: The implementation of the tetrahedral meshing technique was employed for discretizing and dividing the computational domain into tetrahedral elements.
- Solver: The CST simulation utilized the Time Solver method to analyze electromagnetic fields over time within the given computational setup.

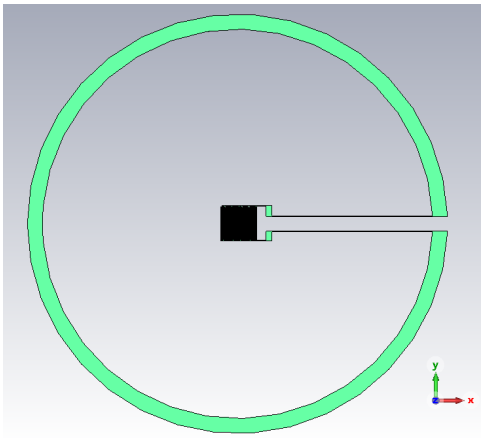

Figure 4.3: Complete Sensor modelled in CST as per Table 3.1

Materials	Available in CST	Young's modulus	Dielectric	Conductivity
PMMA	yes	2.9	4.9	
Polyimde	yes	2.5	3.5	
Molybdenum	yes	120		1.82E+007
SiO_2	yes	75	3.9	
Si_3N_4	no		9.5	
Skin tissue	no		7.29E+1	4.91E-1
Fat tissue	no		1.27E+1	6.84E-2
Muscle tissue	no		6.60E+1	7.08E-1
Copper	yes	120		5.8e+07

Table 4.1: Material Properties in the CST material library

4.1.3. Simulation Set up

Two principal simulations, designated as case 1 (as illustrated in Figure 4.4), resembling an implant antenna configuration tailored for detecting post-surgical infections as described in work by Ararat et al. (2020) [62], and case 2 (shown in Figure 4.6), were setup to assess the resonance shift of the sensor.
An additional simulation, case 3 was conducted utilizing a structure designed to closely resemble the fabricated structure. The purpose of this simulation was to investigate alterations in the resonant frequency concerning variations in applied strain.

Case 1

In Case 1, the simulation exclusively incorporated a singular biological tissue, specifically fat tissue, characterized with sensor set up (Figure 4.3) by varying thickness within the simulation domain shown in Figure 4.4 and its corresponding simplified illustration shown in Figure 4.5.

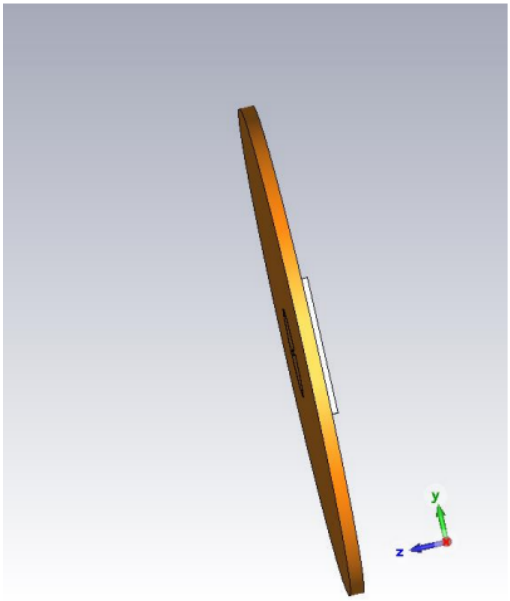

Figure 4.4: Modelled set up seen on CST platform: Case 1

Figure 4.5: Demonstration of the simplified version of the above set up: Case 1

This configuration aimed to provide an initial insight into the sensor's operational functionality at the anticipated frequency. Additionally, it sought to ascertain the sensor's response to escalating fat tissue thickness, consequently augmenting the overall distance between the sensor and the antenna.

Case 2

Within Case 2, three distinct biological tissues—skin, fat, and muscle tissues, as illustrated in Figure 4.6 and its corresponding simplified illustration in Figure 4.7, were incorporated. This case encompassed two specific subcases, wherein the thicknesses of both the fat and muscle tissues were varied, as detailed in Table 4.2.

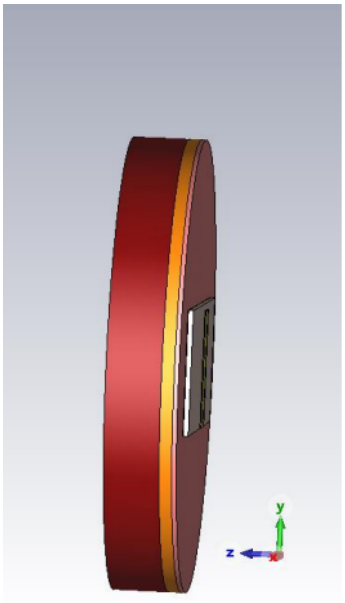

Figure 4.6: Modelled set up seen on CST platform: Case 2

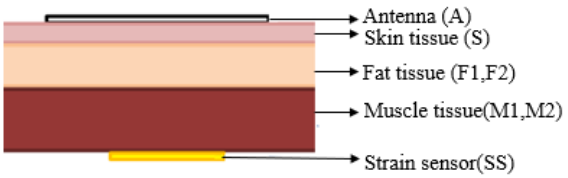

Figure 4.7: Demonstration of the simplified version of the above set up: Case 2

Case2	
	Conditions
i.	Simulated with A,S,F1,M1,SS
ii.	Simulated with A,S,F2,M2,SS

where,	
for i.	S = 0.30cm
	F1 = 0.85cm
	M2 = 2.50cm
for ii.	S = 0.30cm
	F2 = 1.70cm
	M2 = 3.50cm

Table 4.2: Two different conditions of Case 2

Upon confirming that the sensor exhibited the anticipated frequency response in Case 1, subsequent simulations were conducted to investigate how the resonant frequency was influenced when the sensor was implanted within the body and interacted with an external antenna, following the specified conditions outlined in Case 2.

Case 3

In case 3, a simulation closely resembling the characterization setup was employed. The structure, when simulated with the antenna, closely mirrors the design of the fabricated structure. However, due to project time constraints, the fabricated sample (Figure 3.9) does not incorporate the inductor loop (as depicted in Figure 4.3), which was present and simulated in case 1 and case 2. In this scenario, the antenna is simulated alongside the designed structure. (shown in Figure 4.1) as shown in Figure 4.8 and its corresponding simplified illustration shown in Figure 4.9.

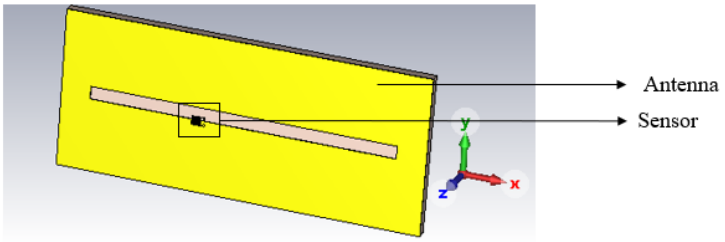

Figure 4.8: Modelled set up seen on CST platform: Case 3

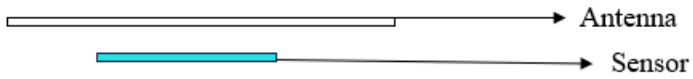

Figure 4.9: Demonstration of the simplified version of the above set up: Case 3

4.1.4. Characterization

Throughout the simulations, slot antennas were consistently employed; however, for the purpose of characterization, a horn antenna was utilized. Horn antennas are known to demonstrate superior directivity and gain in contrast to slot antennas as detailed in the literature [63]. Additionally, due to their physical structure, horn antennas exhibit improved resilience to various environmental conditions like moisture, dust, or temperature fluctuations compared to slot antennas. Furthermore, the fabrication process of horn antennas might be comparatively more straightforward, especially for specific applications, in contrast to the complexities associated with slot antenna designs.

The fabricated strain sensor was subject to characterization using a horn antenna , as illustrated in Figure 4.10, in order to analyze the variations in resonant frequency in response to changes in applied strain.

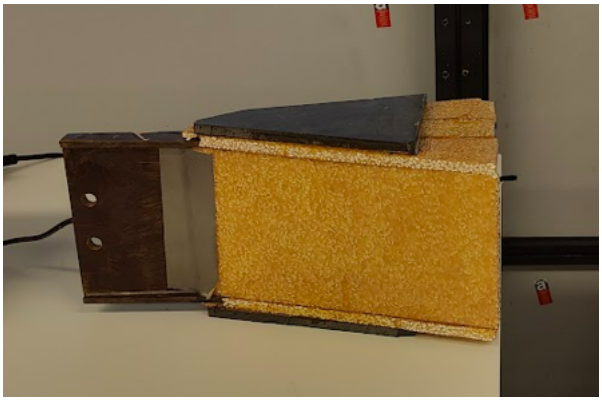

Figure 4.10: Horn antenna

The horn antenna used has a range from 100 MHz to 4 GHz. Figure 4.11 demonstrates the antenna setup employed to characterize the strain sensor samples. A Keysight P9374A Network Analyzer has been employed to gather the results to extrapolate the antenna's data, illustrated in Figure 4.12.

Figure 4.11: Horn antenna set up with the sensor

Figure 4.12: Keysight P9374A Network Analyzer

4.2. Results

The outcomes derived from the simulation configurations delineated Section 4.1.3 are detailed below.

4.2.1. Simulations Set up

The simulation solely encompassed the antenna situated within the fat tissue, without the inclusion of the fabricated sensor intended to exhibit strain variation. In this specific scenario, the resonant peak was identified at 0.40 GHz as seen in Figure 4.13.

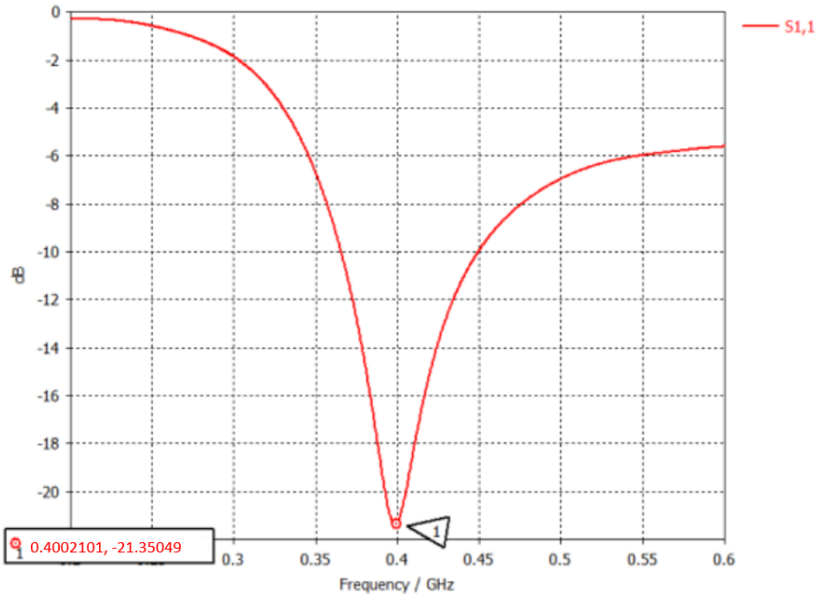

Figure 4.13: S11 parameters when only antenna was simulated

As outlined in Section 4.1.3, two distinct cases were investigated for simulations. The primary objective was to comprehend how the resonant frequency would alter, concerning the variations in the thickness of one or more biological tissues. The varied parameters and corresponding results have been compiled into the tables presented below.

Case 1

The sensor underwent simulation, varying the thickness of fat tissue according to the configuration depicted in Figure 4.4. This approach aimed to comprehend the alterations in resonance shift (in Table 4.3) within the sensor seen in Figure 4.15.

Sr.no	Varying fat thickness (cm)	Resonant frequency (GHz)	Magnitude (dB)
1.	0.68	0.403	-34.21
2.	0.85	0.400	-21.35
3.	1.02	0.396	-17.16
4.	1.19	0.394	-14.85
5.	1.36	0.392	-13.30
6.	1.70	0.390	-11.43

Table 4.3: Changes in resonant frequency with changes in fat tissue thickness

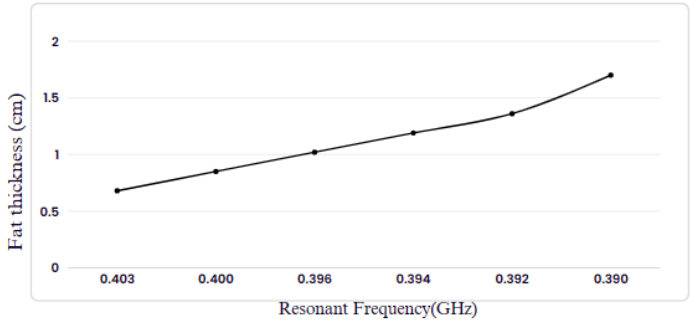

Figure 4.14: Resonant frequency vs fat tissue thickness.

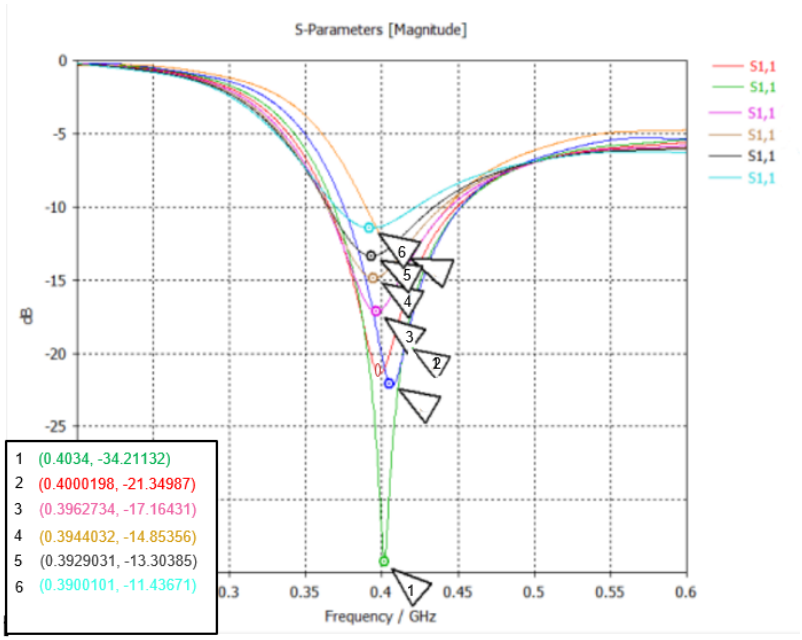

Figure 4.15: S11 parameters when only antenna and sensor were simulated with varying fat tissue thickness.

Sr.no	Varying in Strain (%)	Resonant Frequency (GHz)	Magnitude (dB)
1.	0%	0.400	-21.35
2.	2%	0.37	-21.29
3.	4%	0.35	-21.21
4.	6%	0.34	-21.15
5.	8%	0.32	-21.07
6.	10%	0.31	-20.98

Table 4.4: Changes in resonant frequency with changes in the strain of the sensor

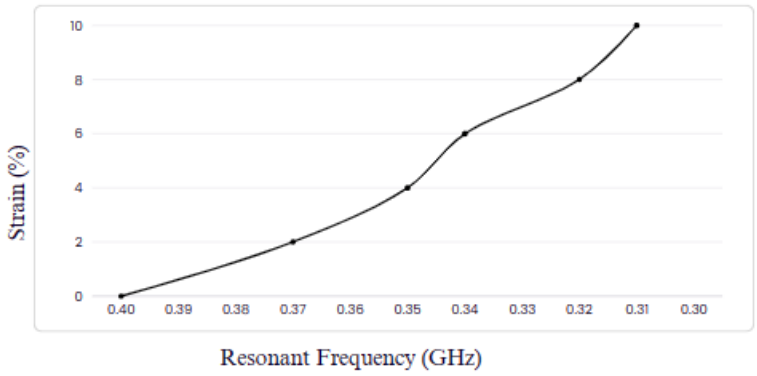

Figure 4.16: Resonant Frequency vs Strain

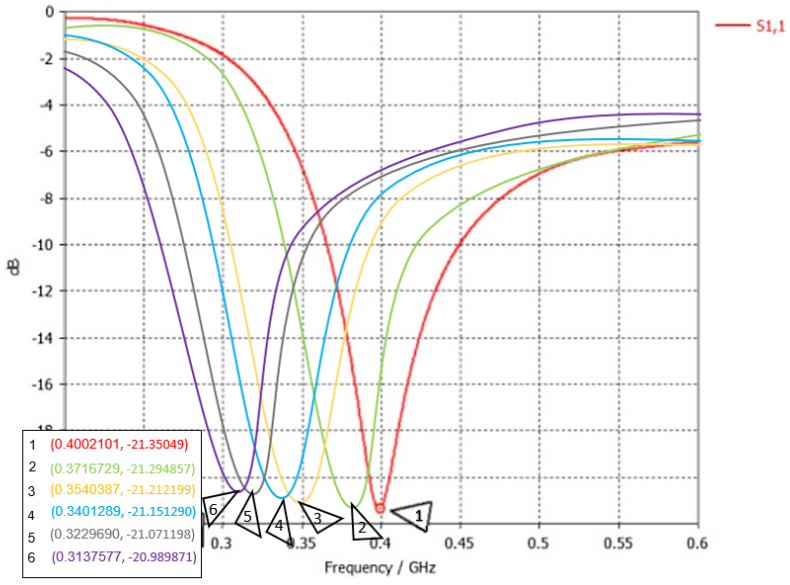

Figure 4.17: S11 parameters when only antenna and sensor with strain variation was simulated

In Table 4.3, alterations in the resonant frequency were observed in relation to increasing fat tissue thickness. A 25% increase in fat thickness corresponded to a 0.74% decrease in the resonant frequency value and a 37.5% decrease in magnitude from the initial value. Subsequently, a 50% increase in fat tissue thickness resulted in a 1.73% decrease in the resonant frequency and a 49.8% decrease in magnitude compared to the initial value. With a 75% increase in fat thickness, a 2.23% decrease was observed from the initial value. Overall, a pattern emerges showing that for each subsequent 25% increase in fat, there is an approximate 22% decrease in the resonant frequency value compared to the preceding value.

In Table 4.4, alterations in the resonant frequency are observed concerning an incremental increase in strain. For a 2% strain increment, a 7.5% reduction in the resonant frequency value and a 0.3% decrease in magnitude are noted. Subsequently, with an additional 2% increase in strain, a further decrease of 5.4% is observed, which is due to the decrease in capacitance value due to deformations. Considering a strain range from 0 to 4%, a cumulative decrease of 12.5% is observed from the original 0.4 GHz value.
Consequently, a 10% strain increase from the original structure demonstrates a 22.5% reduction in the initial resonant frequency value and a 1.8% decrease in magnitude.

Case 2
The simulation focused solely on the antenna's interaction within Skin (S), Fat (F), and Muscle (M) tissues, without the influence of the fabricated sensor intended to demonstrate strain variation. In this specific scenario, the resonant peak was detected at 0.39 GHz, shown in Figure 4.18.

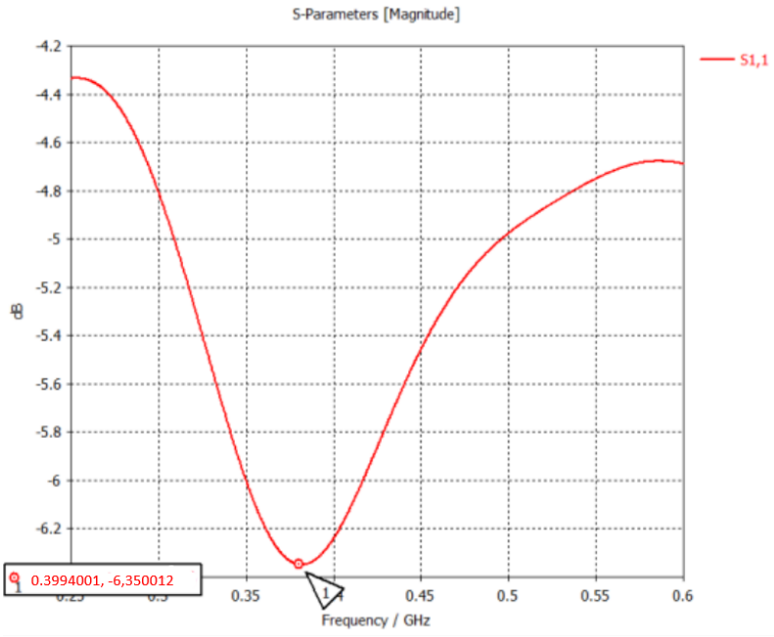

Figure 4.18: S11 parameters when only antenna and biological tissues (skin, fat, muscle) are simulated

The sensor underwent simulation, systematically varying the thicknesses of fat and muscle tissues, following the configuration presented in Figure 4.6 and detailed in Table 4.2. This approach aimed to comprehend the alterations in resonance shift within the sensor.

Sr.no	Conditions	Resonant frequency (GHz)	Magnitude (dB)
1.	A,S,F1,M1,SS	0.38	-6.35
2.	A,S,F2,M2,SS	0.36	-5.31

Table 4.5: Changes in resonant frequency with changes in the fat and muscle tissue thicknesses with Skin(S)= 0.30 cm, Fat (F1)= 0.85 cm and (F2)= 1.70 cm, muscle (M1)= 2.50 cm and (M2)= 3.50 cm respectively.

Within conditions 1 and 2, as delineated in Table 4.5, simulations were conducted for a sensor exhibiting varied strains ranging from 0% to 10%. These simulations involved systematic alterations in the thicknesses of fat and muscle tissues, following the configuration set up presented in Figure 4.6. The primary aim was to comprehend the variations in resonance shift within the sensor (results in Table 4.6) under these different strain conditions seen in Figure 4.19 and Figure 4.20.

Sr.no	Conditions	Strain (%)	Resonant frequency (GHz)	Magnitude (dB)
1.	A,S,F1,M1,SS	0%	0.38	-6.35
		2%	0.37	-6.34
		4%	0.37	-6.30
		6%	0.35	-6.29
		8%	0.34	-6.25
		10%	0.34	-6.23
2.	A,S,F2,M2,SS	0%	0.36	-5.31
		2%	0.35	-5.30
		4%	0.34	-5.14
		6%	0.32	-5.14
		8%	0.32	-5.11
		10%	0.30	-5.07

Table 4.6: Changes in resonant frequency with the changes in fat and muscle tissue thickness and varying strain.

In Table 4.6, alterations in the resonant frequency are observed concerning variations in fat and muscle tissue thickness alongside different levels of applied strain. The total thickness of biological tissues increases by 33.5% between the conditions, as detailed in Table 4.5.

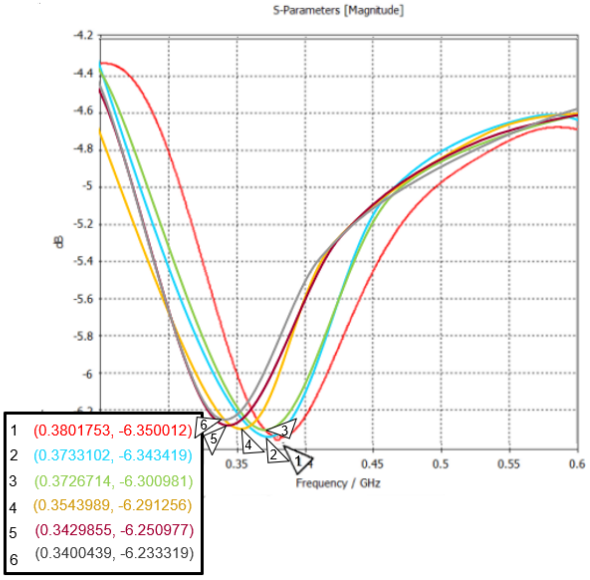

Figure 4.19: S11 parameters when antenna and sensor were simulated with skin, fat (F1) and muscle (M1)

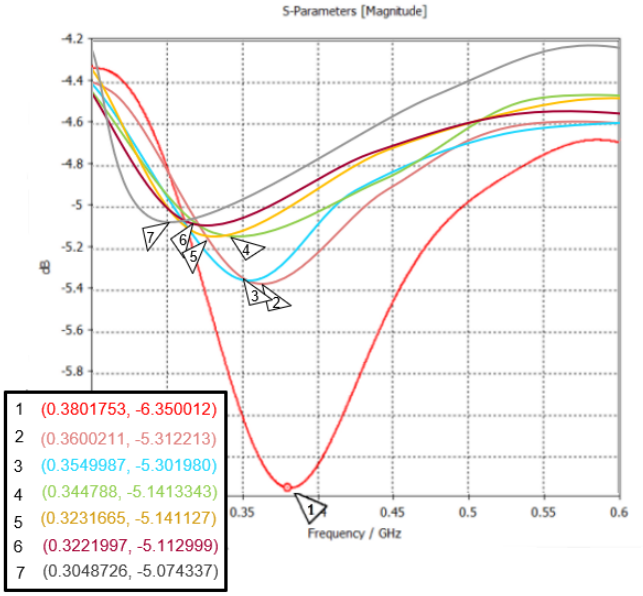

Figure 4.20: S11 parameters when antenna and sensor were simulated with skin, fat (F2) and muscle (M2)

In the first condition, a 2% increase in strain corresponds to a 2.6% decrease in the resonance frequency and a 0.2% decrease in magnitude from the original values. A subsequent 4% strain increase results in a 2.6% decrease in resonant frequency and a 0.79% decrease in magnitude

compared to the original values. Considering a strain of 10%, an overall 10.5% decrease in resonant frequency and a 1.9% decrease in magnitude are observed compared to the original values. In condition 2, a 2% strain increase leads to a 2.8% decrease in the resonance frequency and a 0.2% decrease in magnitude from the original values. A subsequent 4% strain increase results in a 5.6% decrease in resonant frequency and a 3.2% decrease in magnitude compared to the original values. Considering a strain of 10%, there is an overall 16.7% decrease in resonant frequency and a 4.5% decrease in magnitude compared to the original values.

Comparing the 0% and 10% strain between both conditions, there is a 5.3% decrease and an 11.8% decrease in the resonant frequency and a 16.3% decrease and an 18.7% decrease in magnitude, respectively, between both conditions.

Case 3

Further simulations were conducted using six distinct structures, each corresponding to varying strain levels as depicted in Figure 4.1. These simulations involved the use of a slot antenna. The table provided serves to elucidate the values obtained from the characterization results when assessing the structure with the antenna configuration displayed in the setup (Figure 4.11).

Strain	Resonant frequency (GHz)	Magnitude (dB)
0%	1.62	-19.38
2%	1.60	-17.27
4%	1.57	-15.97
6%	1.40	-14.21
8%	1.34	-13.20
10%	1.20	-13.05

Table 4.7: Changes in resonant frequency with the changes in varying strain of the structure shown in Figure 4.1

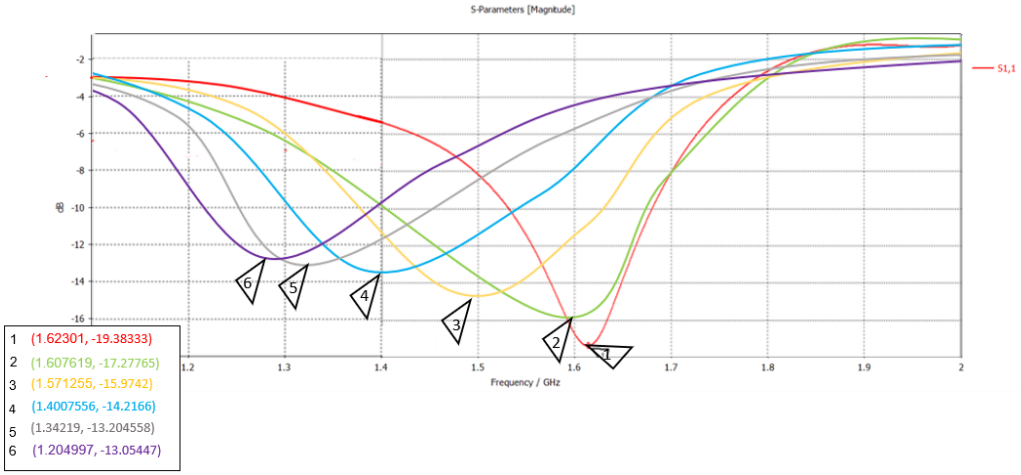

Figure 4.21: S11 parameters when antenna and the capacitor structure shown in Figure 4.1 were simulated

With a 2% increment in strain, a corresponding reduction of 1.2% in resonant frequency and an 11% decrease in magnitude from the intial values are observed. Following a subsequent 4% increase in strain, there is a resultant decline of 3.1% in resonant frequency and a 17.6% decrease in magnitude relative to the initial values. Upon reaching a strain of 10%, a comprehensive reduction of 26% in resonant frequency and a 33% decrease in magnitude are evident compared to the original measurements. This demonstrates a direct correlation between an increase in strain and a subsequent decrease in the resonant frequency.

4.2.2. Characterization with antenna

As mentioned in the Section 4.1.4, the horn antenna was used to characterize the strain structure shown in Figure 3.9 (based on design Figure 4.1)using the set up shown in Figure 4.11. All the 6 sensors of varying strain was measured and the following results were seen (Figure 4.22). The results are combined into the Table 4.8.

Strain	Resonant frequency (GHz)	Magnitude (dB)
0%	1.475	-79.12
2%	1.451	-83.33
4%	1.400	-76.89
6%	1.261	-73.57
8%	1.233	-78.95
10%	1.111	-69.11

Table 4.8: Results from the characterization of the fabricated sample using horn antenna

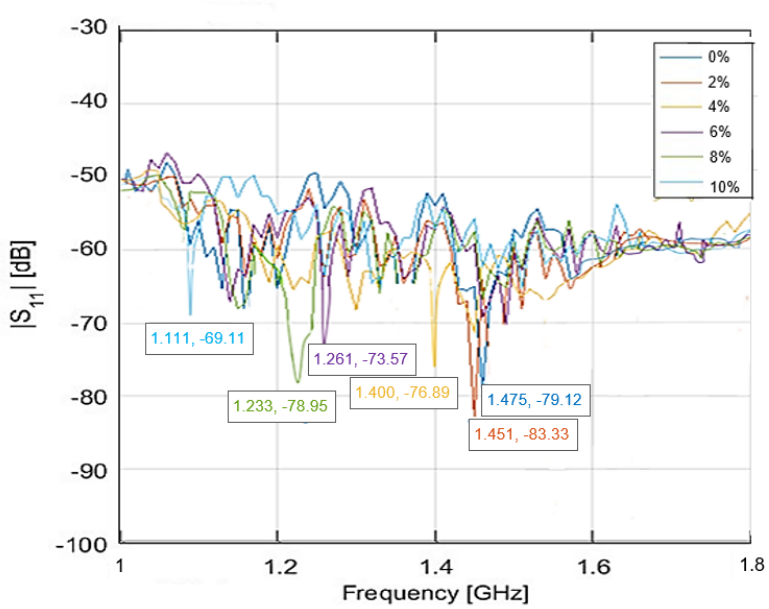

Figure 4.22: Sensor resonance peak shift induced by applied strain

In Table 4.8, variations in the resonant frequency value are observed concerning changes in strain. Different structures exhibiting different strains are characterized using a horn antenna.

During the plotting process for characterization purposes, a specific plot was generated without a sample under evaluation. Subsequently, the outcomes obtained from these plots without samples were utilized by subtracting them from the results obtained after characterizing the antenna with six distinct samples. This subtraction was performed to eliminate external factors that might have influenced the setup during the characterization process.

With a 2% increase in strain, there is a 1.6% decrease in the resonant frequency from the original value. Subsequently, with an additional 2% increase in strain, there is a 3.5% decrease in frequency. Upon reaching a 4% strain increase, a 5.1% decrease in the resonant frequency from the original value is observed. Considering a strain of 10%, a significant 25% decrease is seen in the resonant frequency compared to its original value.

4.3. Discussion

4.3.1. Simulations on CST

The findings presented in Table 4.3 confirmed the operational frequency of the designed sensor to be consistent at the anticipated 400 MHz, seen in Figure 4.15. The narrow bandwidth observed at the resonant frequency implies a heightened selectivity of the antenna or device specifically at that frequency. This narrow bandwidth is indicative of a high quality (Q) factor. Furthermore, the table serves to corroborate the sensor's functionality at the designated frequency of 400 MHz. Additionally, it establishes a correlation revealing that as the thickness of the fat tissue layer increases, resulting in an augmented distance between the sensor and the antenna, there is a proportional decrease in resonant frequency.

The outcomes presented in Table 4.4 depict simulations involving the sensor subjected to varied strains in conjunction with the antenna. Notably, no variation in fat tissue thickness was observed within these simulations. Consequently, the relationship portrayed in this context is solely based on analyzing the frequency shift resulting from the variation in strain illustrated in Figure 4.16, while maintaining a constant thickness of the fat thickness layer. This constancy in fat layer thickness ensures no alteration in the distance between the sensor and the antenna.

The outcomes obtained from Table 4.7 were derived through simulations aimed at establishing correlations with the results obtained during characterization. A notable frequency shift was observed with an incremental rise in strain. Notably, during simulations where the distance between the antenna and the sample was increased, a discernible shift in the resonant frequency was observed. This observation may contribute to elucidating the difference in values between the simulated results in Table 4.7 and the measured outcomes in Table 4.8.
The results from the tables illustrate a notable trend: a higher percentage decrease in frequency is observed with variations in strain. However, it's important to note that substantial frequency shifts necessitate not only variations in strain but also changes in the thickness of the tissue material. Both factors, strain variation and tissue thickness, collectively contribute to observing significant shifts in frequency.

A model approximating the human body was constructed, incorporating skin, fat, and muscle tissues (Figure 4.6). This setup aimed to replicate a similar environment to when the sensor would be implanted within the body system. The sensor, showcasing varied strains, underwent

simulation alongside the antenna, with constant skin thickness and varying fat and muscle tissue thicknesses. As illustrated in Table 4.6, the initial operating frequency was determined to be 390 MHz (Figure 4.19 and Figure 4.20). Notably, an increase in strain resulted in a reduction in resonant frequency. However, the bandwidth exhibited a lower value, indicating a low Q factor. The higher attenuation, measured at -6 dB, of the transmitted signal through these layers indicates increased losses in transmission pathway. These losses predominantly stem from the absorption, reflection, and scattering of electromagnetic waves as they interact with and traverse through the skin, fat, and muscle tissues [64].

The increased dB loss implies a reduction in the effectiveness of signal transmission or reception and indicates a wider bandwidth or decreased selectivity around the resonant frequency. This phenomenon suggests a diminished sensitivity of the system to the desired signals owing to the influence of absorption and scattering effects induced by the additional layers.

4.3.2. Characterization

Probable Hypothesis:
Given the utilization of a slot antenna tuned to 0.40 GHz in the simulations, the anticipated results for characterizing the sensor under varied strain conditions using the slot antenna setup should ideally fall within the approximate range of 0.38 GHz to 0.42 GHz.

However, due to the ease of availability, a horn antenna was utilized. The frequency range of the horn antenna was notably higher, spanning between 0.4 GHz and 4 GHz, which significantly surpasses the range of the slot antenna.

Obtained results:
The outcomes of the characterization process are displayed in Table 4.8. By utilizing a horn antenna for the sensor's characterization, as hypothesized previously, a frequency range shift was observed. The observed frequency range lies within 1-1.5 GHz (Figure 4.22). Although this range does not align precisely with the predicted values mentioned in the hypothesis, the overall trend identified in the simulations in Section 4.2.1 persists and is substantiated by the characterization results.

Discrepancies between simulated and measured results are apparent when characterizing the antenna with the sensor (Table 4.4 and Table 4.8) and the antenna with the structure (Table 4.7 and Table 4.8).
The dissimilarities observed in Table 4.4 and Table 4.8 could potentially be attributed to the presence of a substantial inductor coil, depicted in Figure 4.3, possessing significant inductance. However, the fabricated structure (Figure 3.9 as per the design in Figure 4.1 lacks this inductor loop, resulting in a notable shift in the resonance frequency. A comparison between the simulated 0% strain value in Table 4.4 and the measured 0% strain value in Table 4.8 reveals this discrepancy. Nonetheless, the overarching pattern of decreasing resonant frequency with increasing strain persists.
Both the designed structure, illustrated in Figure 4.1, and the fabricated structure, shown in Figure 3.9, share similar designs (no inductor loop). Simulated results indicate a resonant fre-

quency range between 1.2 GHz and 1.65 GHz, while characterization results exhibit a range of 1.1 GHz to 1.5 GHz. A shift of 0.15 GHz between the simulated and measured 0% strain results is noticeable, potentially attributable to the loaded resonant frequency, which pertains to the antenna's resonance when coupled with the structure. Changes in the structure's strain, notably alterations in the gap distance between the interdigits (here), can impact the antenna's electrical properties, dielectric constant, and impedance, thereby affecting its resonant frequency.

Moreover, differences in the distance between the antenna and the structure during simulation and characterization, owing to the utilization of distinct antennas, might also contribute to the observed frequency shift. Nonetheless, it is imperative to note that despite these discrepancies, the trend of frequency decrease remains consistent between simulated and characterized results.

A noticeable alteration in the resonant frequency occurs concomitantly with changes in strain. Both simulation and characterization outcomes indicate a decrease in the resonant frequency as strain levels increase.

These findings underscore the operational functionality of the strain sensor, affirming its capability to detect early implant failures. Moreover, it signifies the potential of this sensor as a diagnostic tool for healthcare practitioners, offering valuable insights for informed decision-making in the realm of rehabilitation and recovery following hip implant surgery.

5

Final Remarks

5.1. Discussion

It was determined that alterations in strain induced changes in capacitance, consequently causing a shift in the resonance frequency of the sensor. Upon applying a 2% strain, a calculated decrease of 1.1% in capacitance and a 7.5% reduction in the resonant frequency value were observed. With a 10% strain, a calculated capacitance decrease of 4.7% coincided with a shift in frequency from 0.4 GHz to 0.31 GHz in the simulation data. Despite observing a similar trend between the simulated and measured data, indicating a decrease in resonant frequency with increasing strain, disparities exist between the simulated and measured results. These discrepancies might stem from using different antennas during simulations and characterization.

Consistently observed throughout all simulation and characterization results is a pattern linking changes in strain to alterations in the resulting capacitance value. This change in capacitance is directly associated with a shift in resonant frequency, offering insight into variations in strain. Therefore, the shift in resonant frequency serves as a valuable indicator for understanding and assessing strain variations. The capability to detect strains across a range from 0 to 10% signifies the alignment within a favorable range conducive to stimulating osteogenesis. To fulfill the requisite standards, the sensor necessitates construction entirely using biodegradable materials, encompassing both the electrical circuits for sensing and passive wireless transmission. The fabrication of the sensor involved the utilization of biocompatible materials to ensure compatibility post-implantation, thereby mitigating any adverse reactions within the body.

5.2. Conclusion

In summary, the LC circuit was designed and manufactured with a specific target at its potential application in hip implants. Its functionality aimed to detect strains ranging from 0 to 10%, serving dual purposes: early detection of potential implant failures and serving as a diagnostic tool for healthcare providers to make informed decisions regarding rehabilitation and recovery post-hip implant surgery.

Overall, the fabricated devices exhibited outcomes comparable to those simulated using CST Microwave Studio.

5.3. Future Works

In vivo biodegradability studies serve as a crucial means to comprehensively comprehend and evaluate the performance, degradation kinetics, biocompatibility, and physiological effects of the sensor within the body. These studies typically involve animal models to assess the degradation rate of the biodegradable sensor. Surgical implantation of the sensor into specific anatomical sites within the animal body enables the monitoring of the degradation process.

Observation and analysis are conducted using imaging modalities or microscopic examination of tissue samples, alongside assessments of alterations in mechanical properties. Furthermore, the byproducts resulting from degradation are scrutinized to understand the involved metabolic pathways and ensure their non-toxicity and compatibility with the body's natural metabolic processes.

An essential aspect of these studies involves evaluating tissue responses post-implantation to identify any adverse reactions, inflammatory responses, or tissue damage attributed to the degrading material. Favorable outcomes from *in vivo* studies play a pivotal role in advancing the development of a biodegradable, biocompatible strain sensor for clinical implementation in hip implants. Subtle modifications in the sensor's design, such as employing a serpentine-structured interdigitated layout instead of the interdigitated design featured in this project, could prove beneficial in discerning microstrains more effectively. After the fabrication stage, additional encapsulation of the sensor with a biodegradable elastomer can be employed. This step aims to prevent the formation of micro cracks within the metal-patterned electrodes during the sensor's fabrication process.

The use of a biodegradable elastomer for encapsulation is intended to ensure that the stretchability of the sensor, a critical factor in its fabrication and design, remains unimpaired. This encapsulation process with a biodegradable elastomer is anticipated to maintain the sensor's stretchable properties while safeguarding against potential micro crack formation in the metal electrode patterns.

References

[1] Elise B.E. Raney and Andrea M. Spiker. “Chapter 9 - Hip Anatomy and Biomechanics”. In: *The Female Athlete*. Ed. by Rachel M. Frank. Elsevier, 2022, pp. 113–130. ISBN: 978-0-323-75985-4. DOI: https://doi.org/10.1016/B978-0-323-75985-4.00027-1. URL: https://www.sciencedirect.com/science/article/pii/B9780323759854000271.

[2] *Anatomy of the hip*. URL: https://www.muhealth.org/conditions-treatments/orthopaedics/hip-pain/anatomy-of-the-hip.

[3] Jeffrey N. Katz, Kaetlyn R. Arant, and Richard F. Loeser. “Diagnosis and Treatment of Hip and Knee Osteoarthritis: A Review”. In: *JAMA* 325.6 (Feb. 2021), pp. 568–578. ISSN: 0098-7484. DOI: 10.1001/jama.2020.22171. eprint: https://jamanetwork.com/journals/jama/articlepdf/2776205/jama_katz_2021_rv_200017_1612545232.7026.pdf. URL: https://doi.org/10.1001/jama.2020.22171.

[4] Andrew R. Beadling, Anne Neville, and Michael Bryant. *Degradation of metal hip implants*. Jan. 2023, pp. 41–74. DOI: 10.1016/b978-0-12-821596-8.00006-9. URL: https://doi.org/10.1016/b978-0-12-821596-8.00006-9.

[5] Hospital For Special Surgery. *X-ray of a total hip replacement*. Nov. 2019. URL: https://www.hss.edu/condition-list_hip-replacement.asp.

[6] A. Jurewicz et al. “No Association between Genetic Variants of the COMT and OPRM1 Genes and Pain Perception among Patients Undergoing Total Hip or Knee Arthroplasty for Primary Osteoarthritis”. In: *Genes* 13 (2022). DOI: 10.3390/genes13101775.

[7] Liam Ives et al. “Conformable and robust force sensors to enable precision joint replacement surgery”. In: *bioRxiv (Cold Spring Harbor Laboratory)* (Aug. 2021). DOI: 10.1101/2021.08.19.456934. URL: https://doi.org/10.1101/2021.08.19.456934.

[8] Ilya Reviakine. “Implant integration: Problems at the interface”. In: *Biointerphases* 11.2 (June 2016). DOI: 10.1116/1.4952652. URL: https://doi.org/10.1116/1.4952652.

[9] Mythili Prakasam et al. “Biodegradable Materials and Metallic Implants—A review”. In: *Journal of Functional Biomaterials* 8.4 (Sept. 2017), p. 44. DOI: 10.3390/jfb8040044. URL: https://doi.org/10.3390/jfb8040044.

[10] Muhammad Iqbal Sabir, Xiaoxue Xu, and Li Li. “A review on biodegradable polymeric materials for bone tissue engineering applications”. In: *Journal of Materials Science* 44.21 (Aug. 2009), pp. 5713–5724. DOI: 10.1007/s10853-009-3770-7. URL: https://doi.org/10.1007/s10853-009-3770-7.

[11] Lili Tan et al. “Biodegradable Materials for Bone Repairs: A Review”. In: *Journal of Materials Science and Technology* 29.6 (2013), pp. 503–513. ISSN: 1005-0302. DOI: https://doi.org/10.1016/j.jmst.2013.03.002. URL: https://www.sciencedirect.com/science/article/pii/S1005030213000558.

[12] Xiaojian Wang et al. “Topological design and additive manufacturing of porous metals for bone scaffolds and orthopaedic implants: A review”. In: *Biomaterials* 83 (Mar. 2016), pp. 127–141. DOI: 10.1016/j.biomaterials.2016.01.012. URL: https://doi.org/10.1016/j.biomaterials.2016.01.012.

[13] Xiangyu Zhang, Gang Fang, and Jie Zhou. “Additively Manufactured Scaffolds for Bone Tissue Engineering and the Prediction of their Mechanical Behavior: A Review”. In: *Materials* 10.1 (Jan. 2017), p. 50. DOI: 10.3390/ma10010050. URL: https://doi.org/10.3390/ma10010050.

[14] Mohammad J. Mirzaali et al. “Additive Manufacturing of Biomaterials—Design Principles and their Implementation”. In: *Materials* 15.15 (Aug. 2022), p. 5457. DOI: 10.3390/ma15155457. URL: https://doi.org/10.3390/ma15155457.

[15] Amir A. Zadpoor. “Additively manufactured porous metallic biomaterials”. In: *Journal of Materials Chemistry B* 7.26 (Jan. 2019), pp. 4088–4117. DOI: 10.1039/c9tb00420c.

[16] Yageng Li et al. “Additively manufactured biodegradable porous metals”. In: *Acta Biomaterialia* 115 (Oct. 2020), pp. 29–50. DOI: 10.1016/j.actbio.2020.08.018. URL: https://doi.org/10.1016/j.actbio.2020.08.018.

[17] Prithivirajan Sekar, S. Narendranath, and Vijay Desai. “Recent progress in in vivo studies and clinical applications of magnesium based biodegradable implants – A review”. In: *Journal of Magnesium and Alloys* (Jan. 2021). DOI: 10.1016/j.jma.2020.11.001. URL: https://doi.org/10.1016/j.jma.2020.11.001.

[18] Bernd Wegener et al. “Development of a novel biodegradable porous iron-based implant for bone replacement”. In: *Scientific Reports* 10.1 (June 2020). DOI: 10.1038/s41598-020-66289-y. URL: https://doi.org/10.1038/s41598-020-66289-y.

[19] Girish Chandra, Ajay Pandey, and Sushrut Pandey. “Design of a biodegradable plate for femoral shaft fracture fixation”. In: *Medical Engineering and Physics* 81 (July 2020), pp. 86–96. DOI: 10.1016/j.medengphy.2020.05.010. URL: https://doi.org/10.1016/j.medengphy.2020.05.010.

[20] Sina Naddaf Dezfuli et al. “Advanced bredigite-containing magnesium-matrix composites for biodegradable bone implant applications”. In: *Materials Science and Engineering: C* 79 (Oct. 2017), pp. 647–660. DOI: 10.1016/j.msec.2017.05.021. URL: https://doi.org/10.1016/j.msec.2017.05.021.

[21] Yageng Li et al. “Additively manufactured functionally graded biodegradable porous iron”. In: *Acta Biomaterialia* 96 (Sept. 2019), pp. 646–661. DOI: 10.1016/j.actbio.2019.07.013. URL: https://doi.org/10.1016/j.actbio.2019.07.013.

[22] Andrew Burton, Peng Sun, and Jerome P. Lynch. “Bio-compatible wireless inductive thin-film strain sensor for monitoring the growth and strain response of bone in osseointegrated prostheses”. In: *Structural Health Monitoring* 20.3 (Mar. 2019), pp. 749–767. DOI: 10.1177/1475921719831452. URL: https://doi.org/10.1177/1475921719831452.

[23] Ashraf Darwish, Gehad Ismail Sayed, and Aboul Ella Hassanien. “The impact of implantable sensors in biomedical technology on the future of healthcare systems”. In: *Intelligent pervasive computing systems for smarter healthcare* (2019), pp. 67–89.

[24] Kylie E. Nash, Keat Ghee Ong, and Robert E. Guldberg. “Implantable biosensors for musculoskeletal health”. In: *Connective Tissue Research* 63.3 (Feb. 2022), pp. 228–242. DOI: 10.1080/03008207.2022.2041002. URL: https://doi.org/10.1080/03008207.2022.2041002.

[25] Rujie Sun et al. “Stretchable piezoelectric sensing systems for Self□Powered and wireless health monitoring”. In: *Advanced Materials Technologies* 4.5 (Feb. 2019). DOI: 10.1002/admt.201900100. URL: https://doi.org/10.1002/admt.201900100.

[26] Liu Xu, Wei Yuan, and Yuanying Qiu. “Advanced Flexible Skin-Like Pressure and Strain sensors for human health monitoring”. In: *Micromachines* 12.6 (June 2021), p. 695. DOI: 10.3390/mi12060695. URL: https://doi.org/10.3390/mi12060695.

[27] Meipu Li et al. “Wireless Passive flexible strain sensor based on aluminium nitride film”. In: *IEEE Sensors Journal* 22.4 (Feb. 2022), pp. 3074–3079. DOI: 10.1109/jsen.2021.3138786. URL: https://doi.org/10.1109/jsen.2021.3138786.

[28] Leonardo Lamanna et al. “Flexible Dual-Wave Mode ALN-Based Surface Acoustic wave device on polymeric substrate”. In: *IEEE Electron Device Letters* 41.11 (Nov. 2020), pp. 1692–1695. DOI: 10.1109/led.2020.3025607. URL: https://doi.org/10.1109/led.2020.3025607.

[29] Hongjie Jiang et al. “A wireless implantable strain sensing scheme using ultrasound imaging of highly stretchable zinc Oxide/Poly dimethylacrylamide nanocomposite hydrogel”. In: *ACS applied bio materials* 3.7 (May 2020), pp. 4012–4024. DOI: 10.1021/acsabm.9b01032. URL: https://doi.org/10.1021/acsabm.9b01032.

[30] Flurin Stauffer et al. “Soft Electronic Strain Sensor with Chipless Wireless Readout: Toward Real□Time Monitoring of Bladder Volume”. In: *Advanced Materials Technologies* 3.6 (May 2018). DOI: 10.1002/admt.201800031. URL: https://doi.org/10.1002/admt.201800031.

[31] Jaehong Lee et al. “Stretchable and suturable fibre sensors for wireless monitoring of connective tissue strain”. In: *Nature Electronics* 4.4 (Apr. 2021), pp. 291–301. DOI: 10.1038/s41928-021-00557-1. URL: https://doi.org/10.1038/s41928-021-00557-1.

[32] Shenglong Wang et al. “Bioinspired MXene□Based Piezoresistive Sensor with Two□stage Enhancement for Motion Capture”. In: *Advanced Functional Materials* 33.18 (Feb. 2023). DOI: 10.1002/adfm.202214503. URL: https://doi.org/10.1002/adfm.202214503.

[33] Yuting Cai et al. “A stretchable, conformable, and biocompatible graphene strain sensor based on a structured hydrogel for clinical application”. In: *Journal of materials chemistry. A, Materials for energy and sustainability* 7.47 (Jan. 2019), pp. 27099–27109. DOI: 10.1039/c9ta11084d. URL: https://doi.org/10.1039/c9ta11084d.

[34] Giovanni A. Salvatore et al. “Biodegradable and highly deformable temperature sensors for the internet of things”. In: *Advanced Functional Materials* 27.35 (July 2017). DOI: 10.1002/adfm.201702390. URL: https://doi.org/10.1002/adfm.201702390.

[35] Clementine M Boutry et al. “A sensor measuring deformation and pressure, entirely biodegradable, for orthopedic applications”. In: *2016 IEEE Biomedical Circuits and Systems Conference (BioCAS)*. IEEE. 2016, pp. 144–147.

[36] Clémentine M. Boutry et al. “A stretchable and biodegradable strain and pressure sensor for orthopaedic application”. In: *Nature Electronics* 1.5 (May 2018), pp. 314–321. DOI: 10.1038/s41928-018-0071-7. URL: https://doi.org/10.1038/s41928-018-0071-7.

[37] Rui Yin et al. “Flexible conductive Ag nanowire/cellulose nanofibril hybrid nanopaper for strain and temperature sensing applications”. In: *Science Bulletin* 65.11 (2020), pp. 899–908.

[38] Feifan Sheng et al. “Ultrastretchable organogel/silicone fiber-helical sensors for self-powered implantable ligament strain monitoring”. In: *ACS nano* 16.7 (2022), pp. 10958–10967.

[39] Adeela Hanif et al. “A composite microfiber for biodegradable stretchable electronics”. In: *Micromachines* 12.9 (2021), p. 1036.

[40] Clementine M Boutry et al. “Biodegradable and flexible arterial-pulse sensor for the wireless monitoring of blood flow”. In: *Nature biomedical engineering* 3.1 (2019), pp. 47–57.

[41] Zinnat Morsada et al. “Recent progress in biodegradable and bioresorbable materials: From passive implants to active electronics”. In: *Applied Materials Today* 25 (Dec. 2021), p. 101257. DOI: 10.1016/j.apmt.2021.101257. URL: https://doi.org/10.1016/j.apmt.2021.101257.

[42] Lili Tan et al. “Biodegradable materials for bone repairs: a review”. In: *Journal of Materials Science and Technology* 29.6 (2013), pp. 503–513.

[43] Mladen Veletic et al. “Implants with sensing capabilities”. In: *Chemical Reviews* 122.21 (2022), pp. 16329–16363.

[44] Tiffany Kim et al. “Orthopedic implants and devices for bone fractures and defects: Past, present and perspective”. In: *Engineered Regeneration* 1 (2020), pp. 6–18.

[45] Christian Redlich et al. “Molybdenum – A biodegradable implant material for structural applications?” In: *Acta Biomaterialia* 104 (Mar. 2020), pp. 241–251. DOI: 10.1016/j.actbio.2019.12.031. URL: https://doi.org/10.1016/j.actbio.2019.12.031.

[46] Hung Cao et al. “Development and characterization of a novel interdigitated capacitive strain sensor for structural health monitoring”. In: *IEEE Sensors Journal* 15.11 (2015), pp. 6542–6548.

[47] Darren J Lipomi et al. “Skin-like pressure and strain sensors based on transparent elastic films of carbon nanotubes”. In: *Nature nanotechnology* 6.12 (2011), pp. 788–792.

[48] Hee-Sup Shin and Sarah Bergbreiter. “Effect of finger geometries on strain response of interdigitated capacitor based soft strain sensors”. In: *Applied Physics Letters* 112.4 (2018).

[49] Hussein Nesser and Gilles Lubineau. “Strain sensing by electrical capacitive variation: From stretchable materials to electronic interfaces”. In: *Advanced Electronic Materials* 7.10 (2021), p. 2100190.

[50] Rui Igreja and C.J. Dias. “Analytical evaluation of the interdigital electrodes capacitance for a multi-layered structure”. In: *Sensors and Actuators A: Physical* 112.2-3 (May 2004), pp. 291–301. DOI: 10.1016/j.sna.2004.01.040. URL: https://doi.org/10.1016/j.sna.2004.01.040.

[51] Shidong Ma et al. “Performance of flexible strain sensors with different transition mechanisms: a review”. In: *IEEE Sensors Journal* 22.8 (2022), pp. 7475–7498.

[52] Hsing-Yu Chen and Andrew T Conn. “A stretchable inductor with integrated strain sensing and wireless signal transfer”. In: *IEEE Sensors Journal* 20.13 (2020), pp. 7384–7391.

[53] Filippo Costa et al. “A review of RFID sensors, the new frontier of internet of things”. In: *Sensors* 21.9 (2021), p. 3138.

[54] Santanu Kumar Behera and Nemai Chandra Karmakar. “Wearable chipless radio-frequency identification tags for biomedical applications: A review [antenna applications corner]”. In: *IEEE Antennas and Propagation Magazine* 62.3 (2020), pp. 94–104.

[55] Rong Chen et al. “A critical review of metamaterial in wireless power transfer system”. In: *Iet Power Electronics* 14.9 (May 2021), pp. 1541–1559. DOI: 10.1049/pel2.12099. URL: https://doi.org/10.1049/pel2.12099.

[56] Jing Qin et al. “Flexible and stretchable capacitive sensors with different microstructures”. In: *Advanced Materials* 33.34 (2021), p. 2008267.

[57] Alan J Sangster and Alan J Sangster. “Evolution of compact slot antennas”. In: *Compact Slot Array Antennas for Wireless Communications* (2019), pp. 1–33.

[58] Sonal Dubal and Anjali Chaudhari. “Mechanisms of reconfigurable antenna: A review”. In: *2020 10th International Conference on Cloud Computing, Data Science and Engineering (Confluence)*. IEEE. 2020, pp. 576–580.

[59] Duta Jaizul-Aziz. “Principles of Photolithography in Semiconductor Manufacturing”. In: (2020).

[60] Steffen Diez. “The next generation of maskless lithography”. In: *Emerging Digital Micromirror Device Based Systems and Applications VIII*. Vol. 9761. SPIE. 2016, p. 976102.

[61] Aleksandra Baskakova. “Improved time efficiency for simulation of an antenna for near-field distance measurements in CST studio suite”. In: *2019 Antennas Design and Measurement International Conference (ADMInC)*. IEEE. 2019, pp. 26–29.

[62] Kivanc Ararat et al. “A Biodegradable Implant Antenna Detecting Post-Surgical Infection”. In: *2020 14th European Conference on Antennas and Propagation (EuCAP)*. 2020, pp. 1–4. DOI: 10.23919/EuCAP48036.2020.9135877.

[63] Hirokazu Kobayashi. “Horn antenna”. In: *Analyzing the Physics of Radio Telescopes and Radio Astronomy*. IGI Global, 2020, pp. 144–177.

[64] Sukhmander Singh, Ashish Tyagi, and Bhavna Vidhani. “Physics of Absorption and Generation of Electromagnetic Radiation”. In: *Electromagnetic Wave Propagation for Industry and Biomedical Applications*. IntechOpen, 2021.

A

Appendix

A.1. Case 1 in Simulation Set up

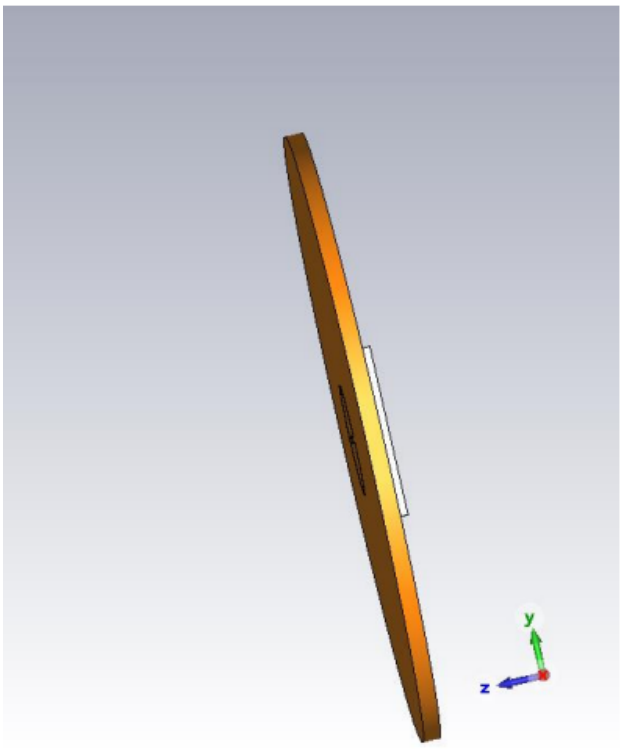

Figure A.1: Side view of the modelled set up with only fat tissue

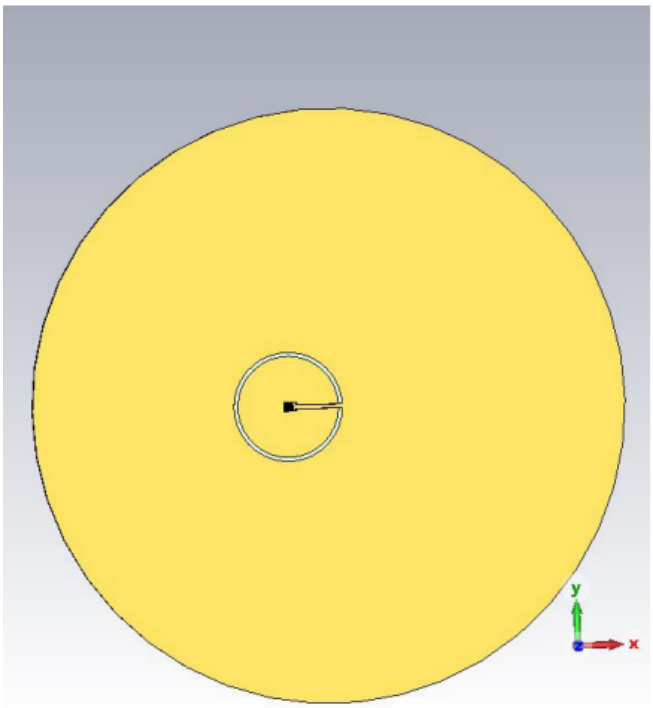

Figure A.2: Top view of the modelled set up with only fat tissue with the sensor visible and the antenna on the opposite side

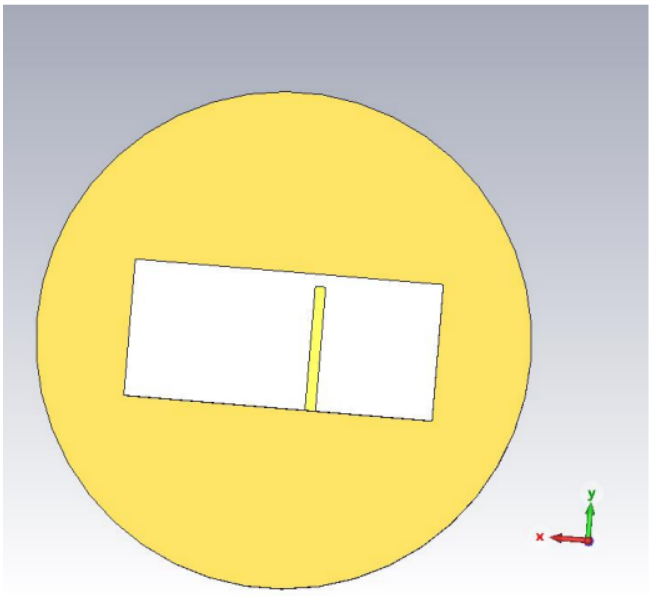

Figure A.3: Top view of the modelled set up with only fat tissue with the sensor antenna and the sensor on the opposite side

A.2. Case 2 in Simulation Set up

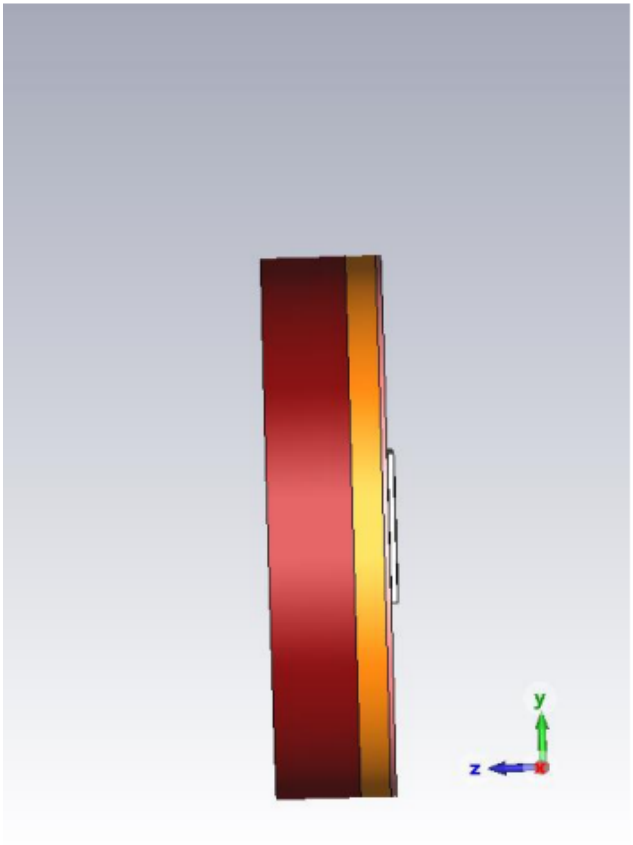

Figure A.4: Side view of the modelled set up with skin, fat and muscle tissues

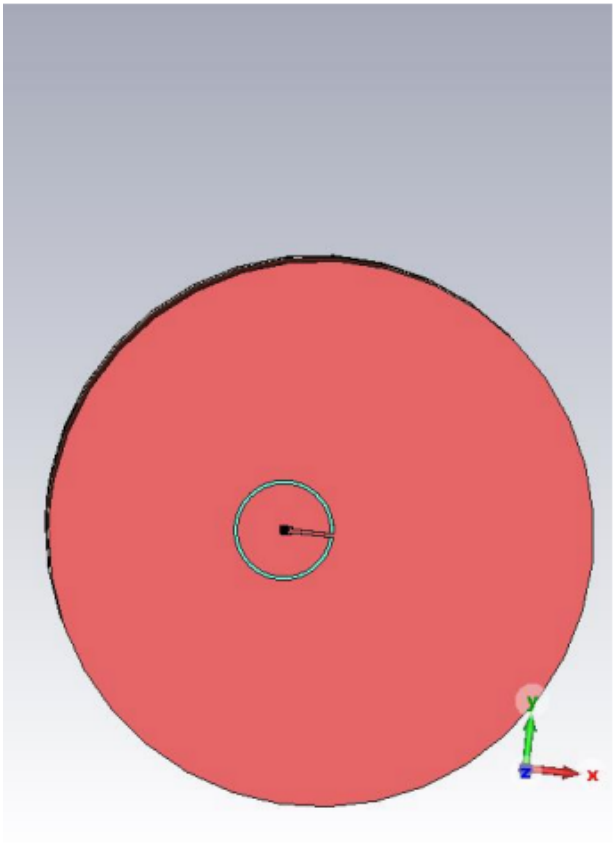

Figure A.5: Top view of the modelled set up with skin, fat and muscle tissues with the sensor visible on the muscle tissue and the antenna on the opposite side (on the skin tissue).